Nanogaps and biomolecules

Chapter 6.

Paolo Motto[*], Ismael Rattalino[*,**], Alessandro Sanginario[*,**], Valentina Cauda[**], Gianluca Piccinini[*], Danilo Demarchi[*,**].

* Politecnico di Torino, Department of Electronics and Telecommunications, Torino, Italy

** Center for Space Human Robotics IIT@Polito, Istituto Italiano di Tecnologia, , , Torino, Italy

Nanogaps and BioMolecules.

Molecular electronic transport characterization is an active part of the research field in nanotechnology. The main underlying idea is to use single molecules as active elements in nano-devices [1]. As a consequence, the proper fabrication of a molecule-electrode contact is a crucial issue [2],[3] and several applications can be thus envisioned. For example, in biosensing it is fundamental the electrochemical detection of different crucial biomarkers upon the investigation and variation of the electric conduction of the metal-molecule-metal junction. Possible applications involve the biomedical diagnostics and the monitoring of biological systems. In particular, the detection of single protein might become the starting point for monitoring drugs, developing clean energy systems, fabricating bio-opto-electronic transistors, and other innovative devices and systems.

The Fabrication of Nanogaps.

NanoGap Electrodes (defined as a pair of electrodes separated by a nanometer-sized gap, NGEs) are fundamental tools for characterizing the electric properties of material at the nanometer scale, even at the molecular scale. They are also important building blocks for the fabrication of nanometer-sized devices and circuits.

Molecular-based devices possess unique advantages for electronic applications with respect to conventional components [4], such as lower cost, lower power dissipation and higher efficiency. Specific molecules can be not only recognized, but also self-assembled on such NGEs, thus leading to elaborated geometries for the study of distinct optical and electronic properties. A variety of specific electronic functions performed by single molecules, including rectifiers [5],[6], switches [7],[8] and transistors [9]-[12], have been designed and studied. Devices based on NGEs [13]-[16], with functional molecules inserted in the desired positions, have great potential as building blocks for super-integrated circuits, and thus can be more likely used in practical applications. Moreover, since the NGEs are fabricated before the molecular component insertion, the junction can be characterized with and without molecules in place, thus facilitating the distinction of the intrinsic molecule properties. As most of the NGEs present a planar configuration, it would be easier to take the underlying substrate as a gate contact to tune the electrical properties of the molecular components. Furthermore, these structures do not require feedback to maintain the mutual arrangement (comparing with conducting tips' Atomic Force Microscope) and are less stochastic with respect to electrochemical cells.

Typical dimensions of target molecules are well below 5 nm, and the fabrication of gaps around this dimension is very challenging, since it goes beyond the capability of traditional microfabrication technologies. In addition, if the gap is too small, molecules can be deposited in a tense and distorted state, resulting in unexpected performances. Several effective and creative methods of fabricating NGEs with controlled spacing were reported in the last few years, including mechanical break junctions [17], electron-beam lithography [18], electrochemical plating [19], electromigration [20], focused ion beam lithography [21], shadow mask evaporation [10], scanning probe and atomic force microscopy lithography [22], on-wire lithography [23], molecular rulers [24].

Electromigration is an advantageous way to fabricate NGEs for nanodevices [25]-[30] and to prepare three-electrode nanodevices with, as example, the substrate as gate [14],[31]. It consists in flowing large density currents in thin metal wires predefined by lithography [32], controlling with a feedback system the value of the driven current. This flowing would cause the electromigration of metal atoms and eventual breakage of the metal wire [33],[34]. This process can yield a stable electrode separation of 1 nm with high efficiency [35] and it can be monitored in real time by observing the current–voltage (I/V) characteristics until only a tunneling signal is present [21],[25],[36].

Technology and Modeling for EIBJ NGE Fabrication

STATE OF THE ART

Electromigration phenomenon consists in the net mass transport generated by the migration of ions inside a conductor material. This is caused by the momentum transfer between conducting electrons and diffusing metal atoms after the application of an electric field. When a current flows in a conductor, the crossing electrons hit the material lattice (scattering phenomenon) randomly. The number of collisions, involving a single ion, depends on the number of electrons going through the conductor (i.e. the electric current density), but also on the temperature at which the phenomenon happens. The accumulation of ions at the anode and the void generation at the cathode can result in nanogap formation.

The relationship between the current density and the temperature is described by the Black's law equation (1) [37]. It is a probabilistic law that gives the MTTF (mean time to failure), usually exploited to establish the reliability of integrated circuits, however it is also useful to understand how it is possible to start the electromigration.

$$MTTF = Aj^{-n}e^{\frac{Q}{kT}} \tag{1}$$

Where A is a constant related to the material geometry, Q is the activation energy for the electromigration in electron volts [eV], K is the Boltzmann constant, T is the temperature in Kelvin degree, j is the medium current density owing in the conductor, n is an exponential factor between 1 and 2 related to the material's type. It has to be noticed that the MTTF presents an exponential reduction with the increasing of the temperature and just a linear reduction with the increasing of the electron density. This is because, when the temperature rises up, there is an increment of the ions' thermal energy and vibrations. Furthermore the ions' vibrations around their reticular positions cause collisions between ions and electrons. Each collision corresponds to a motion quantity transfer from the electron to the ion; if this energy is sufficient, the ion can be detached from the lattice structure generating a vacancy and, in a way similar to the case of the couples electron-vacuum, a flux of ions and vacancies grows up with diffusion inside the conductor. The ions flux is strictly connected to the diffusion term. A constant flux along the conductor, as for instance in a mono-crystal, without any impurities or reticular defects, is not enough for let the electromigration start; in fact for obtaining accumulations and depletions, it is necessary to have a net mass transport between two or more points of the conductor.

Other continuum physical models [38],[39] treat surface electromigration as a moving boundary value problem [40],[41], where mass transport is associated to a surface pattern formation of hillocks and valleys along interfaces and grain boundaries [42]. In other words, electromigration is considered to be a variant of thermal Grain Boundary Grooving (GBG) [43]-[45], where the so-called “electronic wind” enhances the thermal surface diffusion, by transferring kinetic energy to the adatoms during electronic scattering. In the late 50s, Mullins presented a theory [46] that describes the development of surface grooves at the grain boundaries (GBG) of a heated polycrystal. Following this work Rosenberg and Ohring [47] coupled the local surface diffusion at grain boundaries with electronic wind force to model the electromigration evolution. For many years electromigration was treated as a local problem, restricted to grain boundaries, where the influence of the bulk far from interfaces was neglected. In the late 90s, Schimschak et al. [40] proposed a continuum description of surface evolution that considers the non-local coupling between the electromagnetic bulk potential and Mullins’s surface diffusion. Today, some numerical investigations of grain boundary grooving induced by electromigration are based on the level set method [43], where a void initially nucleates at the intersection between a grain boundary and the surface, then moves in the

direction of the current flow, until a second grain boundary is reached. This process is then continuously repeated until gap formation.
During electromigration atoms move from the plane to the film surface, resulting in a reduction of the transverse transport section. If we consider temperature distribution, electromigration likely occurs at the transverse section at highest temperature. This assertion is not valid in any condition [48] but experiments [49],[50] have confirmed this hypothesis is valid where electromigration proceeds slower, as in the first cycle of an R/V curve (Figure 1). An atom by atom depletion was observed by TEM imaging [50] at the beginning of electromigration confined to one grain boundary. A grain boundary is an interface between two grains, or crystallites, in a polycrystalline material, which can be linked to an atomic plane of about 6 x 3 nm^2. At the edges of this surface, the grain boundaries are not involved in electromigration. Moreover, other SEM analyzes [49] confirmed a layer-by-layer electromigration dynamics, excluding thermal run-away and melting.

MODELING

As asserted above, the electromigration is mainly dominated by the current density and by the temperature of the wire. Using electromigration as technique for creating nanogaps, the wire has to have optimized geometries to facilitate the phenomenon and make it more controllable. From this point, to avoid a too high input current, it is necessary to have a small section of the wire [11]; moreover, if the section of the wire is too small, the thermal conductance decreases and the temperature of the wire tends to become excessive, leading to the melting of the wire. The authors defined geometry suitable for EIBJ [32], shown in Figure 2 (a).
The study of the R/V curves for the definition of the electromigration model is crucial, as analyzed in [32],[33]. We can consider the grain boundary involved in the first R/V cycle perpendicular to the wire longitudinal direction and to the electric field, as this orientation maximizes the divergence of the flux responsible of the electromigration trigger. This hypothesis is common in literature [51],[52]. The rate of electrical resistance change can be then directly related to the rate of atoms moving from grain boundaries to the film surface, based on experimental data. Assuming the atomic radius of gold [53] we can calculate the number of atoms in the transverse wire section of 2 um x 25 nm, i.e. N ≈ 491300 atoms per cross section in our geometry (Figure 2 (b)). The percentage resistance variation

$$\frac{\Delta R}{R_0} \tag{2}$$

is inversely proportional to the transport section, were R_0 is the initial sample resistance R at t=0. R is generally a function of time during the electromigration steps. Dividing equation (2) by the duration of the cycle Δt, we obtain the experimental atomic flux EAF expressed in atoms/s:

$$EAF = \frac{\Delta R}{R_0}\frac{N}{\Delta t} \tag{3}$$

With our probes [33], electromigration occurs with a bias current of 50 mA, the first cycle duration lasts from 15 s to 30 s and the electromigration atomic flux ranges 100 and 400 atoms/s. On average, trigger voltage is about 800 mV, the duration of the first cycle is about 23 s and the atomic flux is about 250 atoms/s. Comparing the average duration of the cycle with the average duration of the R/V curves cycles, which lasted around 40 min from the first cycle, we can assume the atomic flux calculation to be almost instantaneous. We validated this hypothesis showing matching between the experimental and the numerical flux obtained from the model of Rosenberg and Ohring [47].
The analytical solution of the equation at the grain boundary intersection x=0 leads to an expression for the groove depth, at an arbitrary time t [47]:

$$y(0,t) = \frac{M(B)^{\frac{3}{4}}}{\sqrt{2}\Gamma\left(\frac{7}{4}\right)} - \frac{m(Bt)^{\frac{1}{4}}}{\sqrt{2}\Gamma\left(\frac{7}{4}\right)} \tag{4}$$

Γ is the Euler Gamma function, B is given by the expression,

$$B = \frac{D_s y_s \Omega^2 \nu}{kT} \tag{5}$$

And M is given by,

$$y(0,t) = \frac{FD_s}{D_b y_b \Omega} \tag{6}$$

Where D_s and D_b are the surface and grain boundary diffusion of the gold atoms, respectively, y_s and y_b are the surface and grain boundary tension of gold, respectively, Ω is the gold atomic volume, ν is the gold atomic surface density, k is the Boltzmann constant, T is the local temperature and F is the total electromigration force [32]. The model output is then the time t needed to electromigrate a y(0,t) thin pillar of gold atoms. If we divide y(0,t) by the atomic diameter of gold d_{gold} [53] we obtain the number of atoms which have left the grain boundary at time t. An atomic pillar in a 25 nm thin wire contains around 70 atoms. Dividing by the time spent to electromigrate the pillar, we can calculate the numerical atomic flux NAF. This can be expressed as,

$$NAF = \frac{T_{wire}}{d_{gold}} \frac{1}{t_{pillar}} \tag{7}$$

Where y(0,t) = T_{wire} is the thickness of the gold wire and t = t_{pillar}. Supposing that electromigration in the transverse section occurs pillar by pillar, the NAF is the output of the electromigration model that needs to be compared with the experimental AF. The inputs of the electromigration model are the temperature at the grain boundary and the electric field, on which the electromigration force depends. The electric field can be related to the current density j using the local Ohm law,

$$E = -\nabla V = -j\rho \tag{8}$$

Where V is voltage and ρ the gold resistivity of the sample. The temperature distribution and the current density vary over time during electromigration, as the surface mass transport varies the geometrical dimensions of the wire over time. Based on these considerations we can conclude that the current density j required for the activation of electromigration process is 10^8 A/cm^2 for a gold wire, as confirmed in [54].
Current density depends both on the applied voltage and temperature, whose trend is related to the shape and the geometry of the probe. Both parameters are strictly related to electromigration. When the electromigration process has just started, under a bulk-neck regime the temperature across the wire is required to be constant to ignite electromigration. When the section decreases temperature is still required to be controlled to avoid melting and surface tension effects that can lead to much larger gaps and gold islands formation [55]-[57], even under a few-atom regime. The use of a model that can simulate and predict these physical phenomena is highly required. An easy way to implement this feature is to build an electrothermal model that relates the thermal and the electrical variables as well as computation in a sole electrical circuit domain, like the Spice model reported in [32]. This model is valid both in the first bulk-neck and in the few-atom regime, and physical operation and the corresponding components in the electrical domain can be inter-related based on the following hypotheses:

1. Heat (through variable) → current source.
2. Temperature (across variable) → voltage.
3. Thermal resistance → electrical resistance.

The problem can be easily solved in the electrical domain only. To trim the model we need to analyze the gold wires parameters. First, the wire is divided in n sections with same length (Figure 3(a)). Each wire is modeled with the same circuit for all sections with same component values (Figure 3(b)). The following equation (9) models the thermal resistance in a section (R_T), which is considered as a generic resistor,

$$R_T = \rho_T \frac{l_k}{S_{Au}} \tag{9}$$

where ρ_T is the gold thermal resistivity, l_k is the length of each section, i.e. the ratio between the total wire length and the number of sections, and S_{Au} is the area of the section obtained by multiplying wire thickness and width. We need to take into account also the heat propagation under the wire through the SiO_2 layer, hence we must evaluate the thermal resistance R_{ox} of the SiO_2 layer. This can be calculated with the same equation with the difference that parameters are referred to SiO_2 and the direction is vertical, therefore,

$$R_{OX} = \rho_{OX} \frac{l_y}{S_y} \tag{10}$$

where ρ_{OX} is the silicon bi-oxide thermal resistivity, l_y is the height of the dioxide layer, S_y is the section area obtained by multiplying the length of the single wire section by its width. The current sources, I_{flux} and

G_{DIP} in Figure 3(b), model the heat flux in the single section of the wire. They are related to the thermal power dissipated in the n-th section in the form of electric power P_E,

$$P_E = R_E I_{bias}^2 \tag{11}$$

where R_E is the electrical resistance in the single section of the wire calculated using the wire length and I_{bias} is the current flowing through the whole probe. For completeness we consider the increase of the electrical resistance with temperature using the equation,

$$R_E = R_{E0}(1 + \alpha(T_E - T_0)) \tag{12}$$

where R_E is the electrical resistance of an n-th section, R_{E0} is the electrical resistance of a single section at the room temperature T_0, α is the temperature coefficient of the electrical resistivity and T_E is the temperature of the n-th section of the wire. Finally we obtain,

$$P_E = R_{E0} I_{bias}^2 + R_{E0}\alpha(T_E - T_0) I_{bias}^2 \tag{13}$$

where $T_E = V_x + T_{sub}$. V_x maps the temperature across resistance R_{ox} and T_{sub} is the temperature of the substrate. I_{bias} is the current that activates the electromigration process. Assuming that $T_{sub} = T_0$ we obtain,

$$P_E = R_{E0} I_{bias}^2 + R_{E0}\alpha V_x I_{bias}^2 \tag{14}$$

Equation (14) comprises two separate items, one constant and one variable (V_x), in particular

- $I_{flux} = R_{E0} I_{bias}^2$ models an independent current source.
- $G_{DIP} = R_{E0}\alpha V_x I_{bias}^2$ models a dependent current source.

Finally the T_{sub} voltage source in Figure 3(b) represents the temperature of the substrate under the oxide. Voltage is now a direct function of the probe temperature. From these results we conclude that the complete thermal gradient fully drops on the wire, suggesting that it may easily break at high temperature. To evaluate our model we ran finite element multiphysics simulations with COMSOL™ [33], using different wire length, but larger than the minimum limit for the electromigration (i.e., the Blech length [56]-[58]). The thermal conduction in the wire is given by the stationary Fourier law, coupled with the Joule dissipated heat power,

$$\frac{|\nabla V|^2}{\rho} = -k\nabla^2 T \tag{15}$$

where k is the thermal conductivity [$Wm^{-1}K^{-1}$] and T is temperature, a function of space. The lefthand term of Equation (15) is the Wm^{-3} power dissipated by Joule effect while Equation (15) is related to an infinitesimal point of space. COMSOL™ uses the nodes of the mesh geometry to make a spatial sampling and integrates the equations in the volume using the nodes as points of integration: if sampling is quite dense, the error is negligible. As a result, we obtain the plot shown in Figure 4 that represents the temperature variation in the wire length obtained for an average trigger voltage of 800mV. Figure 5(a) shows the temperature distribution obtained with COMSOL™, along the complete samples geometry, with the mesh used in simulations. These results validate the Spice electrothermal model.

NANOGAP FABRICATION ALGORITHM

With the consideration explained above we can conclude that during electromigration a control of the flow of the atoms based on the probe electrical resistance is possible. In particular the NAF value obtained from our electromigration model can be compared with the experimental value of EAF, from which we obtain that a percentage resistance increase corresponds to a number N of atoms removed in a time interval Δt. From equation (3) we obtain the expression of N to remove a 25 nm atom pillar, corresponding to the thickness of the probe, within each 50 ms electromigration activation window, the quantity $\frac{\Delta R}{R_0}$ needs to be increased by 2%. This feature can be implemented in a algorithm which is also adaptive to the resistance increase ΔR to maintain a constant sensitivity across the whole R(t) range. The algorithm applies a bias voltage V_{bias} that constantly increase by a step ΔV per second and samples all the resistance values within Δt and compares the average value with the last average resistance sample. When $\frac{R(t)-R_i}{R_i}$>0,02, with R_i the average of the last i-th sample, the fabrication process is stopped and restored with V_{bias} decreased to the 85% of its value. This is necessary to avoid the thermal runaway of the process: indeed, if R(t) increases too quickly, a temperature induced positive feedback can overboost atom migration, hence lead to unrecoverable melting of the probe [32]. The amplitude of the step ΔV per second is also reduced by the 5% to better control the electromigration process.

During the few-atom regime, as much as conductance decreases, the number of quantum jumps decreases leading to a minimum of G_0, the quantum conductance, which is defined as,

$$G_0 = \frac{2e^2}{h} = 77{,}6\ \mu S \tag{8}$$

where e is the electron charge and h the Planck constant. G_0 represents the conductance of a single atom of gold placed between two electrodes [59]. After, the few-atom regime tunneling occurs, but its evaluation is difficult to be achieved in a low-cost real-time architecture: tunneling is indeed based on the measurement and evaluation of pico-to-femto Ampère currents, which is out of reach for our system. Therefore, we assume that once the last quantum jump is reached, the nanogap is formed. If the inverse of the quantum conductance, i.e. 13 kΩ, is reached, the last gold atom can be assumed detached and the probe broken.
The current feedback algorithm controls the V_{bias} applied across the probe, gradually increases it over time, and stops the voltage when the resistance exceeds the value of 13 kΩ, which indicates the nanogap is fabricated. The flow-chart of the current feedback algorithm is summarized in Figure 6(b).
The temperature feedback mechanism checks the probe current and uses it as key for a hash table addressed by the wire temperature. The table is obtained from real-time Spice simulations for n nodes. If the actual wire temperature is larger than those obtained from the model, the software reduces the voltage by a certain percentage, hence instantaneously decreasing temperature. n is determined by the number of activations of the first feedback algorithm. For a 6 µm wire divided into n=30 sections, the removal of a single atom pillar corresponds to removing a single section in the electrothermal Spice model. Once a new cycle is initiated the algorithm needs to re-run the electrothermal model simulation with the updated number of nodes. To obtain the same performance in an 8 µm wire, the number of sections n needs to be set to 40. The flow-chart of the temperature feedback algorithm is summarized in Figure 6(c).
To evaluate the outcome of this fabrication process we have analyzed the obtained gap widths with a FESEM microscope. Our process has permitted the fabrication of gaps under 3 nm. The current algorithm is able to efficiently control the electromigration process: we observe that the gap width w is almost constant for a relative long path. The current feedback mechanism enables the fabrication of uniform nanogaps continuously adapting the intervention on the plot, i.e., subsequently reducing the applied voltage step ΔV.
The block diagram of the hardware system for nanogap fabrication is shown in Figure 7. The gold probes are connected to the circuit that receives the signal from the Embedded Linux and generates (by through the Driver Module) the current flow that induces electromigration. The current flowing through the probe is measured by the Measure Module and the value is processed by the Embedded Linux board which implements the algorithms, which in turns controls the current to be injected in the probe.
The FESEM image in Figure 8 shows no gold melting zones and confirms that the temperature feedback mechanism works efficiently.

Characterization of Molecular Wires

There are many studies, focusing on nanodevices, which integrates NGEs with organic molecules (small molecules [60], oligomers [61], polymers [62], fullerenes [63], and biomolecules [64], etc.) or other nanometer-sized components (CNTs [65], nanocrystals [25], etc.).
Before passing to the study of more complex biomolecules, it is interesting to analyze the simplest structure that can be built inside NGEs: the molecular wire.
Oligothiophenes are promising materials in the molecular electronics field [64] being exploited as building blocks for molecular wires [65]-[66], molecular field effect transistors [67], and molecular diodes [68]. They were studied intensively both theoretically [69] and experimentally [70]. These polymeric molecules were exploited as molecular wire when bridging a nanogap for example in [71]. As suggested by its name, a Molecular Wire (MW) is characterized by a long dimension defining the wire and by a small diameter of just some nanometers. Numerous theoretical ideas were used in an attempt to understand the conductivity of one-dimensional systems, where strong interactions between electrons lead to departures from normal metallic (Fermi liquid) behavior. Effects caused by classical Coulomb repulsion (called Coulomb blockade), interactions with vibrational degrees of freedom (called phonons), and Quantum Decoherence, were also found to be important in determining the properties of molecular wires. To be of use for connecting molecules together, MWs need to display some very important characteristics. The molecular ending

groups should be able to connect with the electrodes forming reliable electrical contacts between them. In addition, the molecular ending groups of the MW should be able to connect specifically to certain materials, such as gold metal surfaces, for connections to outside world. MWs should also possess other functional groups able to bind to biomolecules for nanosensors, nanoelectrodes, molecular switches purposes. In addition, the MWs should also be available of pre-determined diameter and length. They should also have covalent bonds to ensure reproducible transport and contact properties. MWs have been demonstrated, either via gold nanoparticles as linkers, or by direct connection through thiolated molecules. A molecular wire simulation was performed with a quaterthiophene in [71]; here the molecule was connected to two gold electrodes for analyzing its behavior under an external electric field. In [72] the conductance of a single oligothiophene molecule was experimentally measured thanks to the Break junction STM (Scanning Tunnel Microscope).
Based on our recent experience [34], we present here our experiments, describing how we executed the molecular deposition inside nanogaps and which were the resulting devices. The first chosen molecule was an octithiophene (Figure 9) and was dissolved (100 nM) in tetrahydrofurane (THF, Chromanorm, >97%), which shows very low conductivity and high volatility. The molecular solution was then deposited on electromigrated gold nanogaps, monitoring the conductance values until complete solvent evaporation. Additional washing steps in THF were also performed in order to remove the physically adsorbed molecules. The dried molecule–deposited nanogaps were then characterized for I/V plots from -1.5 to 1.5 V under dark conditions and at room temperature. I/V curves were also recorded under ambient light illumination and light irradiation from 300 to 700 nm using a Perkin Elmer LS55 fluorescence spectrometer equipped with a remote fiber optic accessory.
Figure 10(a) shows the obtained current-voltage (I/V) plots, while Figure 10(b) shows conductance-voltage (G/V) plots. These characteristics were measured after the octithiophene deposition on 8 different nanogap probes and show the electrical conduction through octithiophene molecules bridging the two gold electrodes. All the I/V plots have the typical non–linear shape of a Me–M–Me (Metal-Molecule-Metal) junction as described above and reported in Figure 10. Below a certain threshold voltage, the current is low and weakly affected by the applied voltage, whereas it increases markedly with the applied voltage over the threshold. The so called “conductance gap” is the region of the voltage comprised between the positive and negative thresholds and can differ from 1 to 2 V in Figure 10. G/V plots of Figure 10(b) are obtained from I/V curves by deriving the current with respect to the applied voltage. The G/V curve shape is a conductance well, where the width of the well coincides with the conductance gap.

Nanogaps for BioMolecules

The study of biomolecules through electrical characterizations as I/V curves, Impedance Spectroscopy, and in general with the measurement of the change of electrical characteristics of the molecules, is a very powerful methodology that presents good performances associated with the possibility of implementing low-cost instruments. The use of nanogaps for the electrical characterization of molecules is perfectly aligned with this approach, and, reaching the nanometric dimension, has an immense potentiality for opening new fields of research and then the realization of innovative systems and applications.

As in the micro-meso scopic level, the use of RNA-DNA, Antigen-Antibody couples, or the analysis of proteins, is always valid. Thank to the use of nanometric electrodes the sensing parameters are improved, but we can consider as main advantage the fact that the analysis at the nanodimension is extracting novel information from the biomolecules, also because we can start to talk of Single Molecule Sensors, where the specific characteristics of a single or of few molecules are obtained.

For these reasons in the next sub-chapters the description of devices based on RNA/DNA and Proteins will be carried out, underlining the sensing principles obtained from the analysis at nanometric level.

DNA and nanogap-based devices

The combination of nanogap arrays with the enzymatic amplification has opened an incredible broad field of opportunity for fabricating high density and sensitive electrochemical/electrical biosensors. In particular, the investigation of DNA hybridization events has important applications in genomics, pharmacology, gene expression, and diagnostics. Conventional detection methods are based on fluorescence [73], electrochemistry [74], enzyme- [75] and nanoparticle-based [76] techniques. However these approaches require a labeling step for the DNA detection, leading to reduced efficiency, multistep analysis, and samples contamination. In contrast, label-free techniques are able to detect the hybridization event in the DNA strand, monitoring the physical and chemical changes originating from the charged nature of the oligonucleotide. Based on this principle, several nanogap-based biosensors were reported in the literature for the ultrasensitive detection of DNA. As already mentioned in this chapter, to afford the detection of both short and long oligonucleotides, a nanogap of approximately 10 nm is required. Therefore top-down approaches, like the already mentioned fabrication techniques, are well suited for low–cost and high yield realization of the nanogap array also for DNA detection purposes. The technology relies on the hybridization of two termini of DNA strands on the two opposite electrodes. In this way, the bridged nanogap shows an enhanced conductance, relying on the native charge transport trough the double helix bridging the nanogap [77], [78]. Roy *et al.* found in particular that the conductance magnitude is linearly dependent on the DNA concentration [79] and they were able to detect a DNA concentration from 1.0 fM to 1.0 pM. Choi and coworkers [80] were able to detect the DNA hybridization with n- and p-channels of a nanogap embedded in a MOSFET (in particular a NeCMOS). They verified that both the dielectric constant and the charge affect the threshold voltage differently in the n-channel, whereas both factors work synergically in affecting the p-channel device, which results in a 4 time increased threshold voltage with respect to the n-channel. In addition, Shen *et al.* [81] fabricated a highly sensitive nanogap array sensor for the label-free detection of single-nucleotide polymorphism down to 0.1 fM. The strategy relies on measuring the nanogap conductance after bridging the nanogap by hybridized DNA and covering it with silver nanoparticles for obtaining a conductive path. This allowed a more sensitive electrical detection with reduced background noise and enhanced mismatch discrimination [79], [81].

By nanoimprinting, Liang and Chou [82] were able to fabricate a 9-nm nanogap detector inside a 45 µm long nanofluidic channel. They were able to linearize and stretch 1.1 kilobase-pair double stranded DNA along the nanofluidic channel and detect in real-time the tunneling current perpendicular to the DNA backbone. However the authors were not able to be sensitive to a single base type of the DNA.

In general the nanogap-based sensor for DNA detection are quickly moving forward for rapid, real-time and parallel DNA analysis, which is of prominent importance for characterizing pathogens, measuring mRNA levels during expression profiling, detecting early cancers, and more in general in portable and point-of-care applications.

Detection of Proteins

Excluding DNA from the family of nanogap biosensors, not so much research was carried out yet, even though the interest in the field is very high. One of the most common methods for trapping biomolecules to the sensing site is the sandwich assay. A bioconjugate, such as an antibody capable of selectively binding the desired target from a solution, is immobilized on a surface. Such sensing surface in then sandwiched with a second selective bioconjugate layer, allowing the detection when the sandwich is tagged with a particle. The work of Chang *et al.* [83] exploited this concept, creating a protein biochip in which DNA was

used as a bio-barcode. Additionally, conjugate magnetic nanoparticles (MNPs) and gold nanoparticles (AuNPs) were bonded respectively with monoclonal antibodies, the target antigen and polyclonal antibodies. The role of AuNPs was to increase the conductivity of the two electrodes (Figure 11(b)). If the target antigen was not present into the sample solution, no sandwich was formed. In contrast, if the antigen was present, a multilayer of AuNPs over the gap surface between the electrodes was formed (Figure 11(a)). The electric current passing through the ``filled'' gap is then evidenced by the presence of the target antigen. The same principle, but in a simpler way, was used by Sing *et al.* [84] and Marcon *et al.* [85] in their works, where immunoglobulin G (IgGs) from human serum is detected by trapping into nanogap IgGs bonded with secondary antibodies labeled with gold nanoparticles.

However, Kim *et al.* [86] showed that it is possible to exploit biomolecular interactions. For example the nanogap biosensors can electrically detect biotin/streptavidin and antigen/antibody pairs without the need of other enhancing mechanism such as gold nanoparticles.

Up to now we omitted a large category of sensor technology: the field effect transistor (FET) method. A lot of sensors already exploit FET mechanism [87] and nanogap biosensing is among them. Nanogap FET biosensors were used for the detection of Avian Influenza (AI) by means of a Self Assembled Monolayer (SAM). The sandwich was composed by silica-binding proteins and the bioreceptor molecule, i.e. the avian influenza antigen [88]. Recently, Im *et al.* [89] designed a complete device for the detection of AI. They used a nanogap dual-gate field effect transistor array, as shown in Figure 12. With the help of silica-binding proteins (SBPs), the authors were able to detect the complex AI antigen-antibody by measuring the drain to source current.

In the 2010 the group of Choi [90] built an analytical model of a generic nanogap FET-based biosensor by solving a 2D Poisson equation. The proposed model can be used as guideline for the optimization of device dimensions and for maximizing the sensitivity of the nanogap-based transistor.

Another very interesting way to use nanogaps for biosensing is the exploitation of the surface-enhanced Raman scattering (SERS) property. When the incident light with a proper frequency interacts with the metal, surface plasmon is created in a region normally less than 10 nm. When Raman active molecules are positioned in these regions, their SERS signals can be dramatically enhanced [91],[92]. In this case nanogaps are of great convenience, being able to bind to organic molecules. Very recently Chen *et al.* [93] used SERS for the detection of four kinds of microorganisms (Figure 13): Bacillus subtilis (B. subtilis), Bacillus magaterium (B. magaterium), Escherichia coli (E. Coli) and Saccharomyces cerevisiae (S. cerevisiae).

Proteins for Bioelectronics

Bioelectronics is a research field of molecular electronics aiming to exploit biomolecules and building electronic devices with new functionalities compared to conventional electronics. Proteins are believed to be a promising class of biomolecules. They carry out numerous functions in living organisms, involving the exchange of electrons between biological partners, such as photosynthesis, metabolic and catalytic reactions. In particular, metalloproteins, which contain one or more metallic active centers, can efficiently transfer electrons by reversibly changing oxidation state of their active site. Because of their natural redox property, a metalloprotein can be considered itself a device, without requiring any specific material or design in addition to serve a function [94].

Proteins, for building devices, can be integrated with an inorganic probing counterpart. The chemical variety on the protein structure makes possible, upon specific functionalization, to self-assembly and anchor other molecules to the protein structures in a desired position. An example of self-assembling is

given by the well-known blue copper azurin, containing a disulfide bridge allowing the protein to chemisorb easily on gold [94]. Another interesting class of proteins is the antibody. Its intrinsic capability of establishing specific binding with target molecules can be used for biodetection. In addition, antibody shows improved stability and reproducibility of chemisorption on artificial structures, useful for building new devices [95].

For these reasons, many efforts have been focused over the last two decades to develop protein-based electronics. Scanning Probe microscopy, in particular, has established as the most suitable method for characterizing the electrical behavior of proteins, adsorbed on inorganic substrates up to the resolution of a single molecule. In the work of Alessandrini *et al.* [96], an ElectroChemical Scanning Tunnel Microscope (ECSTM) was used to probe azurin in a nanogap across the tip and the substrate, which served the function of source and drain gold electrodes of a single molecule transistor. The electrochemical cell of the ECSTM was used to electrochemically gate such a transistor in aqueous environment. Davis *et al.* [97] reported on the electron transport characteristic of azurin, which was investigated by Conductive-probe Atomic Force Microscopy (CAFM) in dry environment. They found two different transfer mechanisms, depending on the applied contact force: at high imposed force, non resonant tunneling was dominant for any voltage tested. In contrast, at moderate force and high voltage, metallic redox states became accessible, thus determining Negative Differential Resistance (NDR) characteristic. Generally, NDR is defined by a peaky I/V curve where the current increases with the increasing voltage up to a maximum, before dropping for higher values of the voltage. The physical origin of NDR in biomolecules is still in debate and many mechanisms were proposed to explain this effect, such as polaron formation, resonance tunneling, conformational changes in the measured molecule, and the presence of molecular redox states [98]. NDR has attracted great interest in the last years, since it includes the existence of bistable states with an on/off ratio, on which many applications can be based, for instance memories, voltage-controlled oscillator, flip-flop and logic circuits [99]. Recently, Mentovich *et al.* [98] verified direct correlation between NDR and redox centers, by comparing transistor effect in case of azurin or apo-azurin deprived from its redox center. In the latter case indeed apo-azurin did not display any NDR signature, in contrast to the former case, which revealed NDR with a peak to valley ratio (PVR) up to 40.

Although the aforementioned properties of proteins are promising features for developing new electronic devices, real applications are restricted by complex probing systems in terms of miniaturization, cost and parallel portability onto a shared substrate. Among planar probing alternatives to scanning probe microscopy, NGEs seems a promising tool. It can be low cost fabricated in form of array, thus allowing portability and mutual connectivity for circuitries, without requiring feedback to control the mutual arrangement.

Mariuccio *et al.* [100] demonstrated one of the first nanogap-metalloprotein based FET in 2005, by self-assembling blue copper azurin inside nanogap, fabricated by electron beam lithography, and providing silver gate electrode on the back of the silicon substrate. They fully characterized the device in terms of source-drain output resistance (I_{ds}/V_{ds}) and gate-modulated transconductance (I_{ds}/V_g), as shown in Figure 14. The nature of conduction was ascribed to sequential hopping between pairs of reduced and oxidized copper redox centers, as shown in Figure 15. This scheme was confirmed by comparison with apo-azurin and zinc-azurin, which in contrast showed much lower conductivity and no dependence from gate voltage (Figure 14). Transconductance characteristic exhibited a pronounced resonant peak, changing from positive to negative values with a PVR of 2. In other words, the molecular device was able to switch from n-MOSFET to p-MOSFET behaviors before and after resonance respectively, which remarkably leads to a complementary logic, tunable on the same device (Figure 14). Here, the gate effect acted as a regulator of

the relative fraction of reduced azurin: at higher V_g values, the fraction of reduced molecules was greater than that of oxidized ones and vice versa, which resulted in lower or higher electron transfer rate, respectively. As the authors remarked, in principle the exploitation of such complementary logic device had three main advantages: decrease of the logic-gate occupation area, reduction of the fabrication complexity, and decay in power consumption.

In the work of Dimonte *et al.* [101], nanogap-metalloprotein based optoelectronic device was fabricated with photoactive proteins. Reaction Center rhodobacter sphaeroidis (RC) and BacterioRhodopsin halobacter salinarum (BR) were inserted by drop casting in nanogaps, previously obtained by electromigration of gold microwires. AFM imaging clearly proved the coupling between RC and NGEs, as shown in Figure 16. I/V measurements on RC were carried out in absence of light and under light radiation in the visible field. In the first case, NDR response with a PVR around 5 was displayed, comparable with similar electrical characterizations performed on RC by scanning probe microscopy. Notably, as soon as the junction was exposed to visible light, the NDR peak vanished and the nature of ET switched from resonant to non-resonant, as shown in Figure 17. This opto-driven switching mechanism was ascribed to charge separation induced by photo-excitation, directly responsible of the NDR inhibition. Charge separation also determined the opto-electronic behavior of BR. Once the protein was drop casted into the nanogap and exposed to three different light wavelengths (red, blue and green), a photo voltage arose from green light, as expected from the absorbance spectra of the protein with a peak around 507 nm. Conversely, the protein resulted insensitive to light exposure at red and blue wavelengths, as shown in Figure 17. As pointed out by the authors, these results on RC and BR molecular junctions can be a starting point for the fabrication of a novel series of opto-electronic transistors, based on light sensitive metalloproteins.

Although several functionalization methods for self assembly were developed over the years, an open issue of nanogap based molecular junctions still remains, i.e. the implementation of effective, reproducible and durable electrical contacts between molecules and metal electrodes [94], [102]. Attempts have been made in order to improve the stability of molecular junction, by focusing both on the molecular side, and on the inorganic counterpart. The latter point of view was adopted by Choi's group [102], who fabricated metalloprotein NDR device by locating several ferritin molecules between Single Wall Carbon NanoTube (SWCNT) NGEs, formed by electrical cutting of SWCNT (Figure 18). CNT nanogap showed much improved stability over time and reproducibility among different samples, with more than 90% of fabricated devices showing similar behavior. This repeatability was related to the nature of the chemical interaction between the protein and the CNT, which is based on hydrogen bonds among amino acid residuals of ferritin and carboxylic and hydroxyl groups of CNT wall (Figure 18(a)). Interestingly, the device showed a peculiar hysteretic NDR behavior with a PVR around 40, which appeared only in one scan direction of voltage, whereas it disappeared in the opposite direction (Figure 19). The origin of the NDR behavior was ascribed to the redox states of the Fe atom, which involved reduction of Fe(III) and oxidation of Fe(II) during voltage scan. The relation between NDR and redox activity was finally confirmed by a series of control experiments with apo-ferritin deprived of its redox center, which did not exhibit any NDR.

Another approach to improve the molecular junction stability is by exploiting the intrinsic binding capability of antibodies to perform bioelectronics. Chen *et al.* [103] fabricated a protein transistor made of an immunoglobulin G antibody (IgG) binding two gold nanoparticles, which in turn were connected to source and drain of NGEs (Figure 20). IgG is a Y-shaped molecule that consists of three domains: two 'arms' called Fab fragments and a 'stalk' called F_c fragment. The Fabs are connected to the F_c by flexible chains of amino acids, which allow the IgG to bind a broad range of antigens and form a highly stable and reproducible molecular junction between protein and nanogap (Figure 21). This structure was named Pro-T by the

authors. Thanks to the high binding capability of antibody, a secondary IgG was bonded to the primary IgG (Pro-T + IgG'), and a CdSe quantum dot was in turn bonded to the F_c domain of the secondary IgG (Pro-T + QD-IgG'). On the contrary, it was also possible to reduce structural complexity by using Pepsin to digest and remove the F_c fragment from the primary IgG antibody (Pro-T $(Fab')_2$). All these three variants were fully characterized as transistors by measuring transconductance (I_{ds}/V_{ds}) and output resistance (I_{ds}/V_g) characteristics, in dependency of temperature and hydration as shown in Figure 22. The level of hydration did not remarkably affect the efficiency of conduction, whereas an increase of temperature of 100 K enhanced the measured current up to 300% at high bias. NDR signature appeared for negative values of V_{ds} with a PVR proportional to the number of molecular F_c domains: PVR was about 100 for 2 F_c domains, 50 for 1 F_c domain and none in Pro-T $(Fab')_2$ (Figure 23). From this evidence, the authors inferred a direct correlation between the presence of redox states in the F_c domain and NDR behavior of the device. In particular, they claimed that although IgG is not recognized as a redox enzyme, functional groups on the F_c domain might serve as temporary electron acceptors and cause the NDR in the measurement. The presence of the CdSe quantum dot in the form Pro-T + QD-IgG' promoted the modulation of conduction in dependence of the light wavelength similarly to phototransistors, as shown in Figure 24. Finally, the authors found that the incorporation of Horseradish peroxidase (HRP) as conjugated secondary IgG (Pro-T + HRP-IgG') enhanced this photo gate effect by 40%, as shown in Figure 24(b).

Conclusions

As described in this chapter, the use of nanogaps is a very powerful tool and a lot of possibilities are open to the research yet.

A good number of works have been based on DNA molecules, and few studies have beencarried out up to now based on the exploitation of protein functionalities, both for sensing and for bioelectronics. However there is a very wide range of interesting biomolecules with distinctcharacteristics to be exploited in a nanogap device. The use of the new nanometric tools, as nanogaps, will be of great interest for extracting electrical characteristics not yet known from biomolecules or for improving for example the resolution in the analysis of already known behaviors.

As a clear consequence of these innovative results, the biomolecular research can today open new fields of study and bring an enormous increase in the fabrication of novel devices, and in a second step, of new systems and applications.

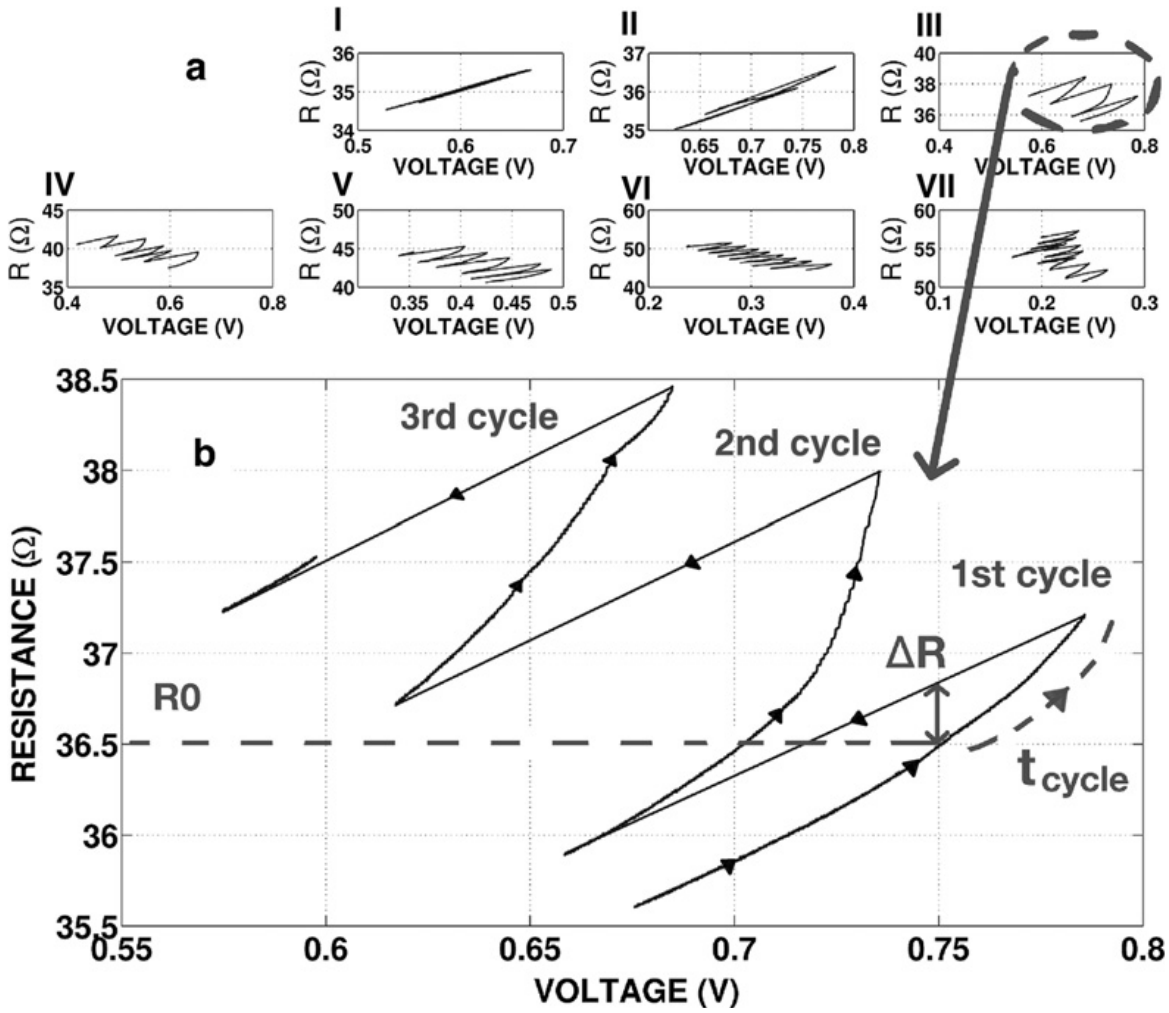

Figure 1: Resistance–Voltage (R–V) plot of the feedback algorithm. (a) 7 windows indicated by roman numerals describe the time evolution of the fabrication process. In the first two windows the increase in resistance is linear and no matter depletion occurs. Joule heating increases resistance with voltage and temperature, then resistance returns to the same values after the voltage drops. Electromigration occurs in the third window, indicated by the circle. (b) Third window magnification, showing the first, second and third cycles. Time direction is indicated by the arrows in the line. [33]

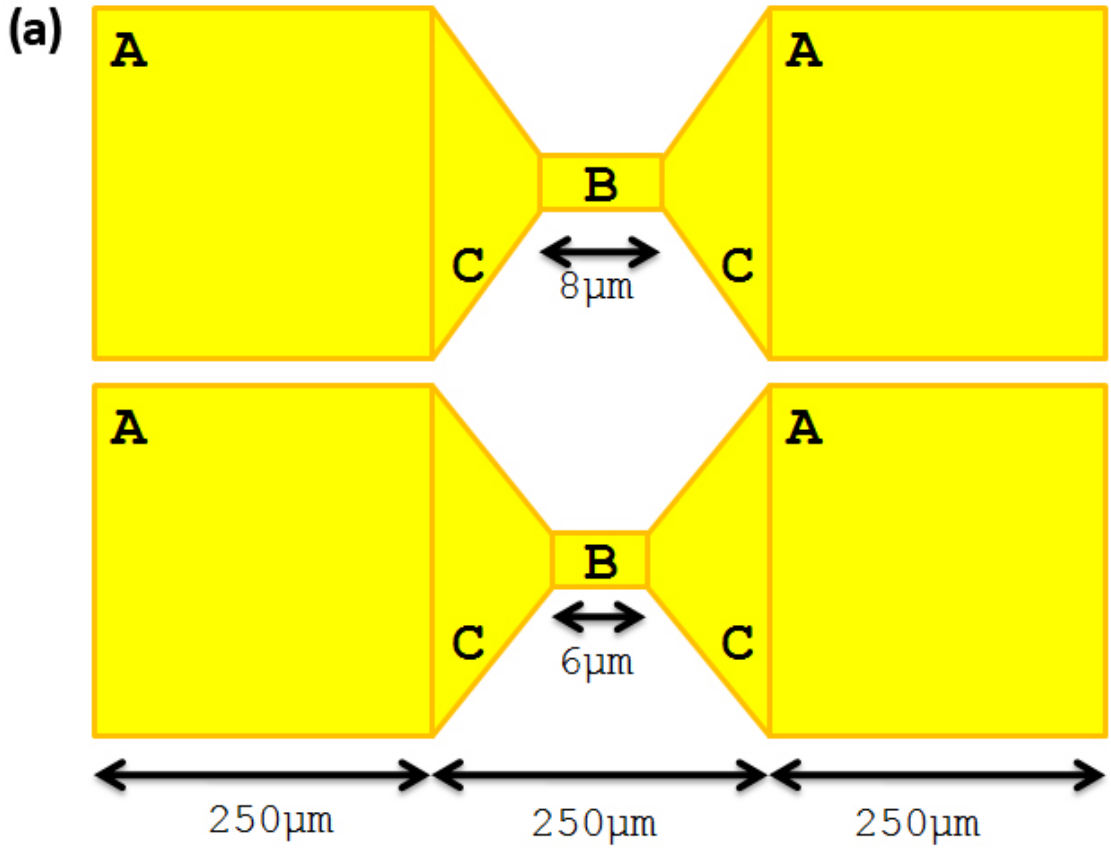

Figure 2: Nanogap probe geometry. (a) Layout. (b) Cross-section;

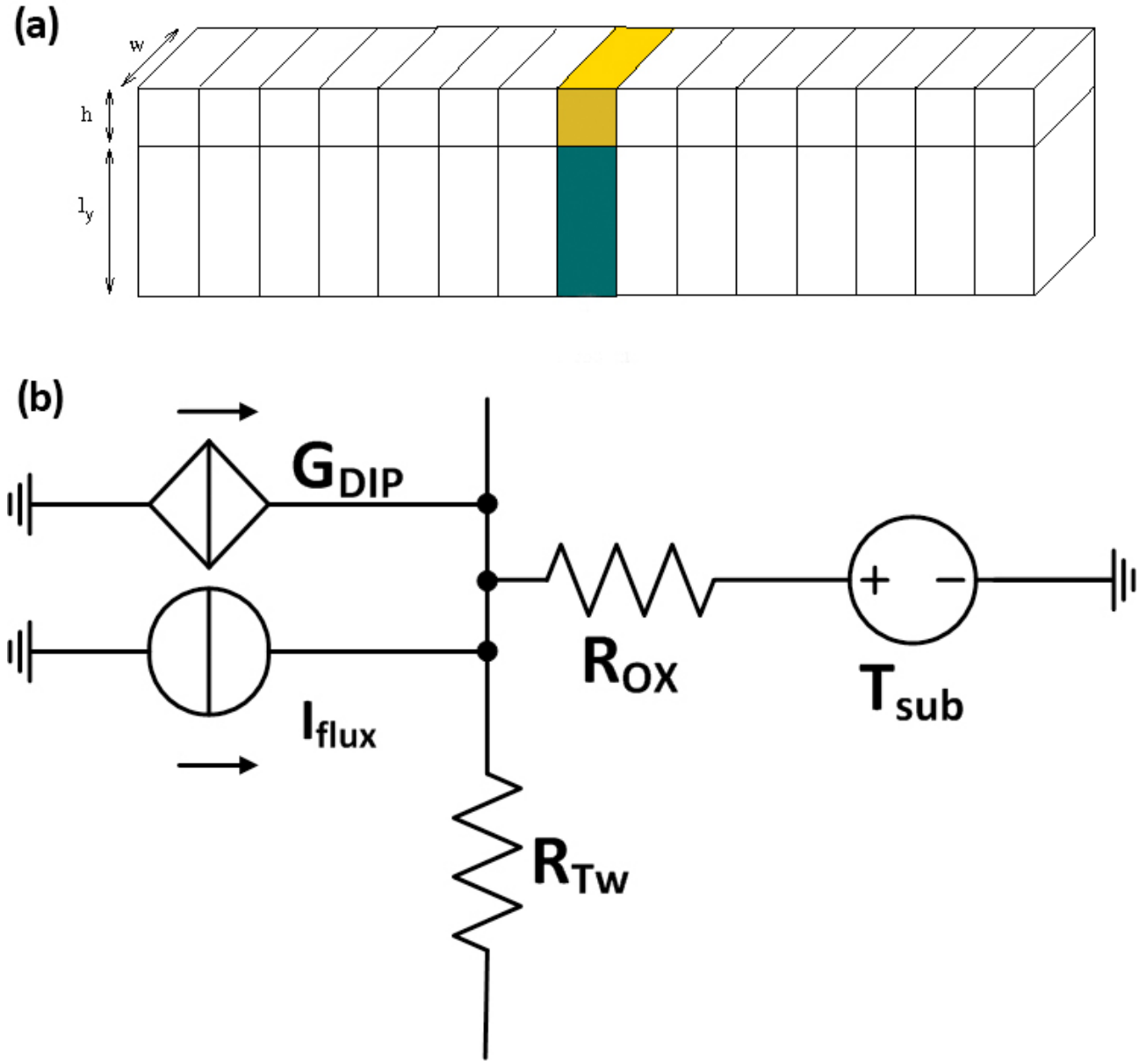

Figure 3: Spice electrothermal model. (a) Wire sections. (b) Electrical circuit equivalent model of a wire section;

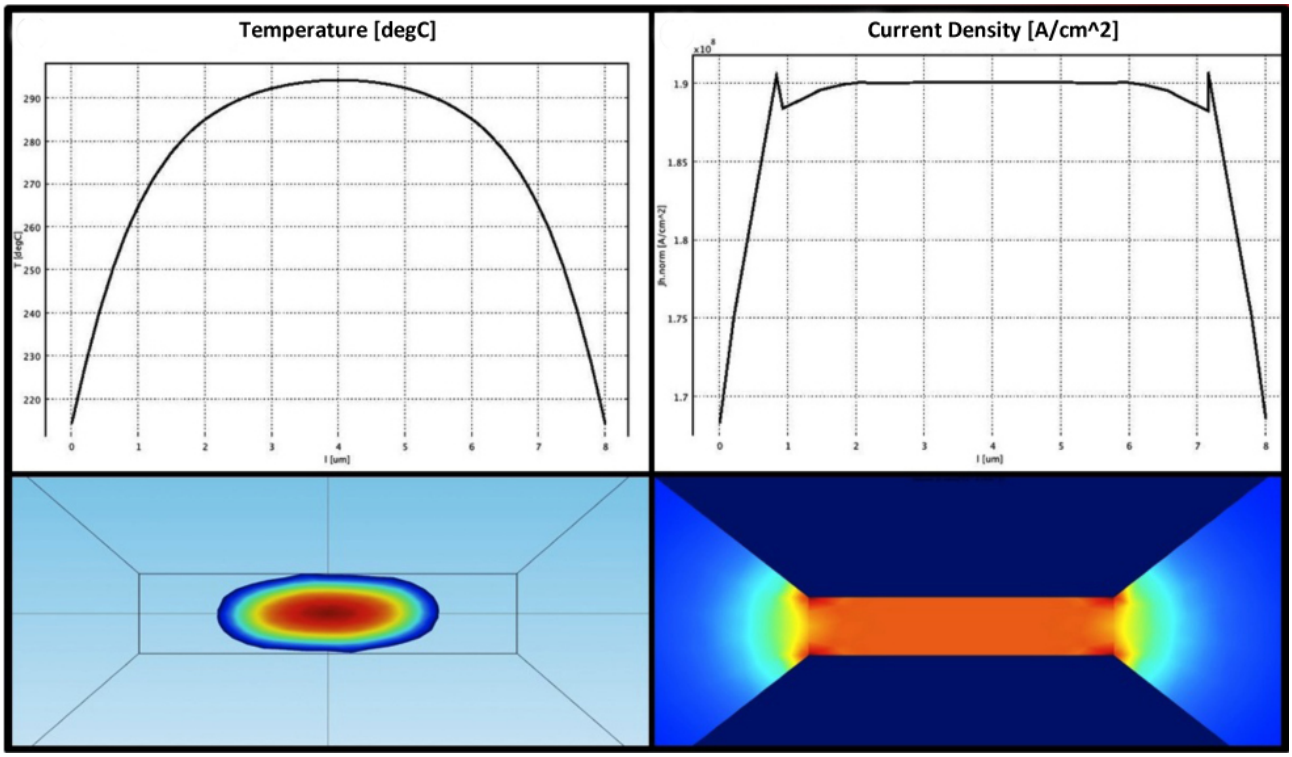

Figure 4: COMSOL™ Electrothermal model [34];

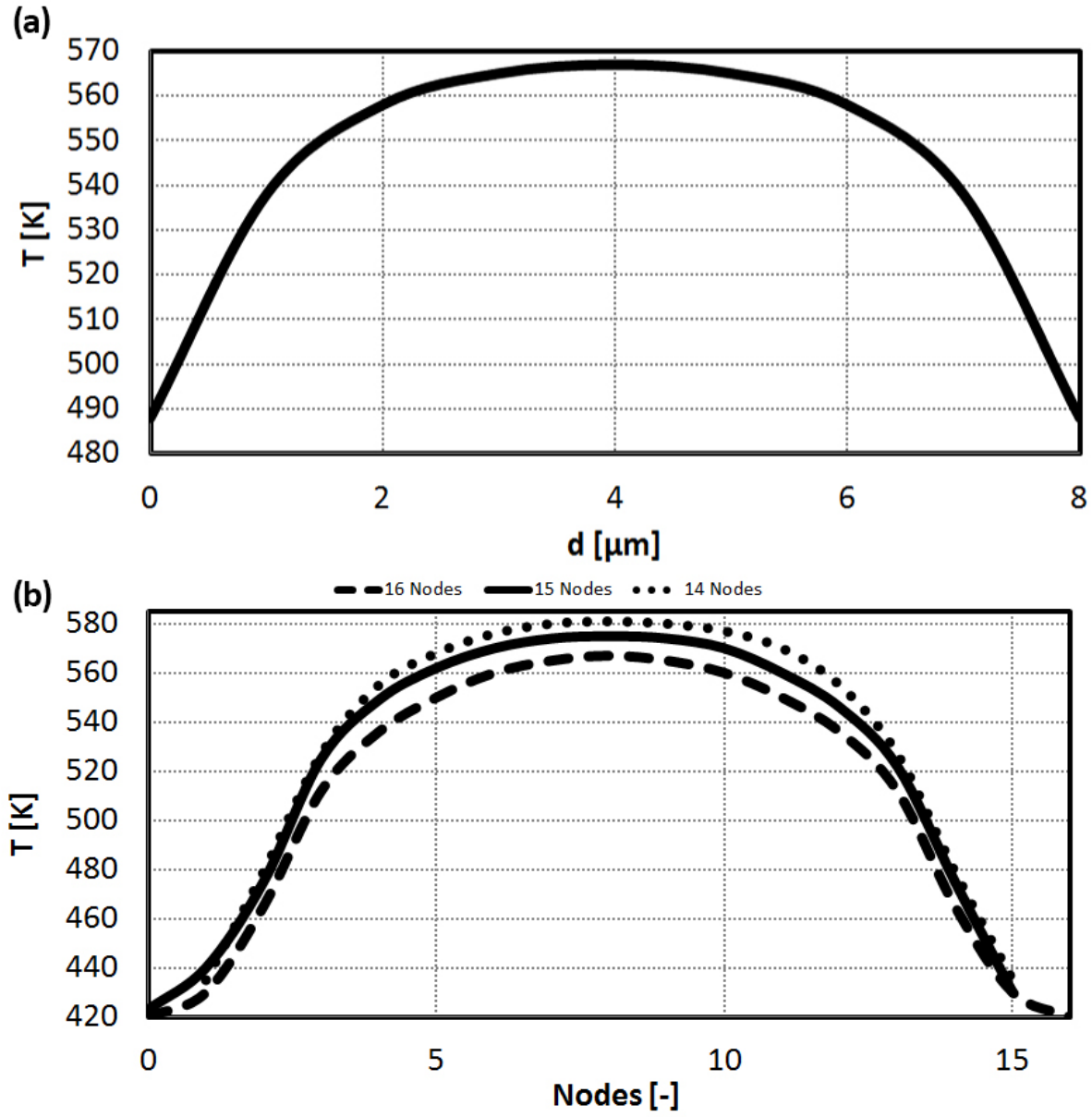

Figure 5: Plots of Electrothermal simulation. (a) COMSOL™ model. (b) Spice model;

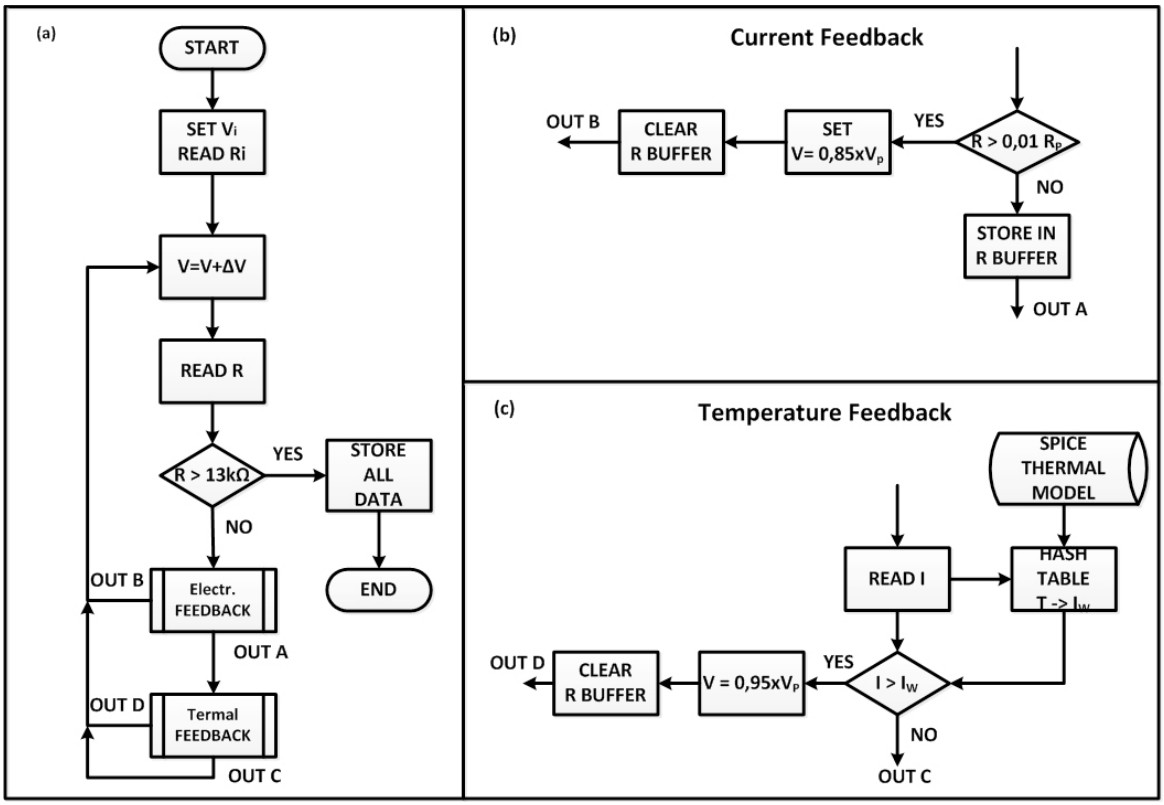

Figure 6: (a) Electromigration process Flow Chart. (b) Current Feedback. (c) Temperature Feedback

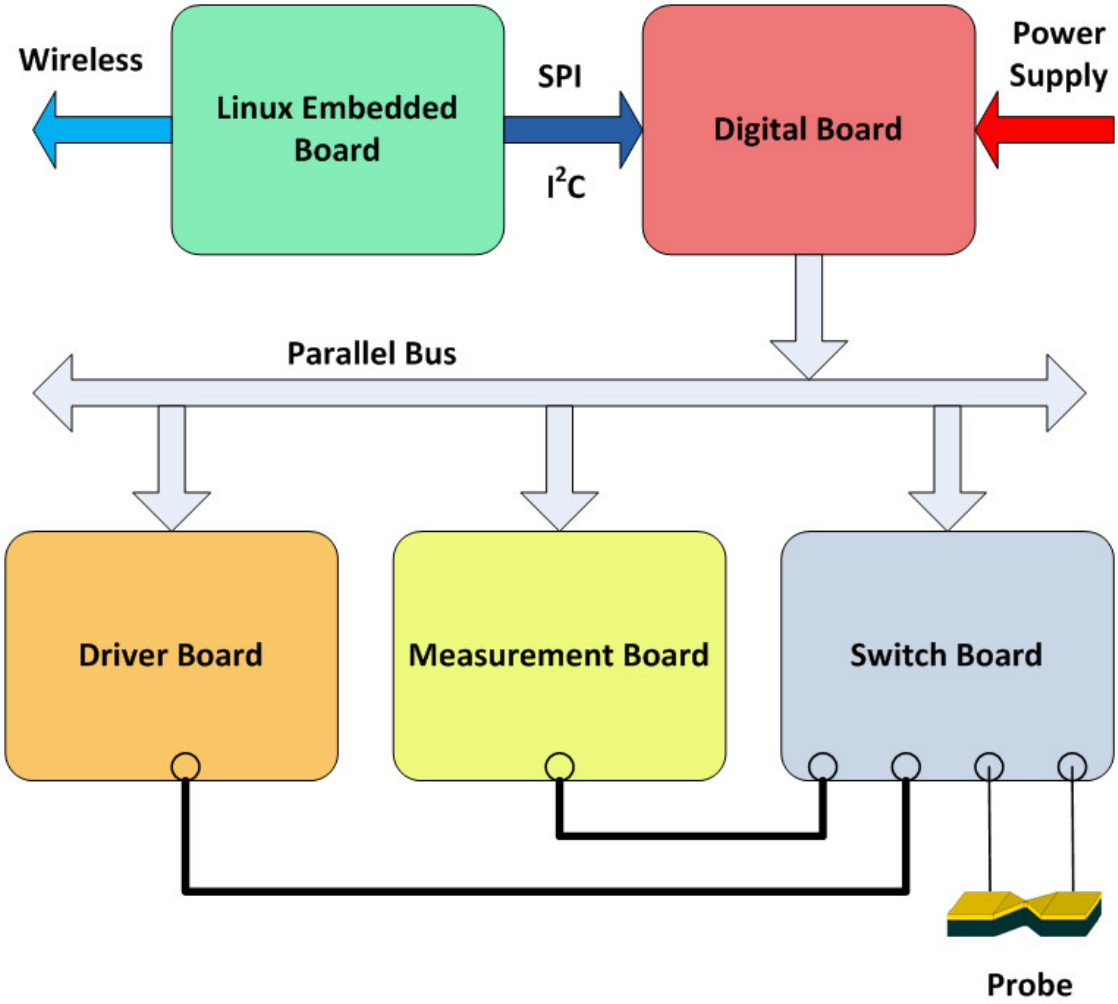

Figure 7: Hardware for EIBJ Nanogap fabrication [34].

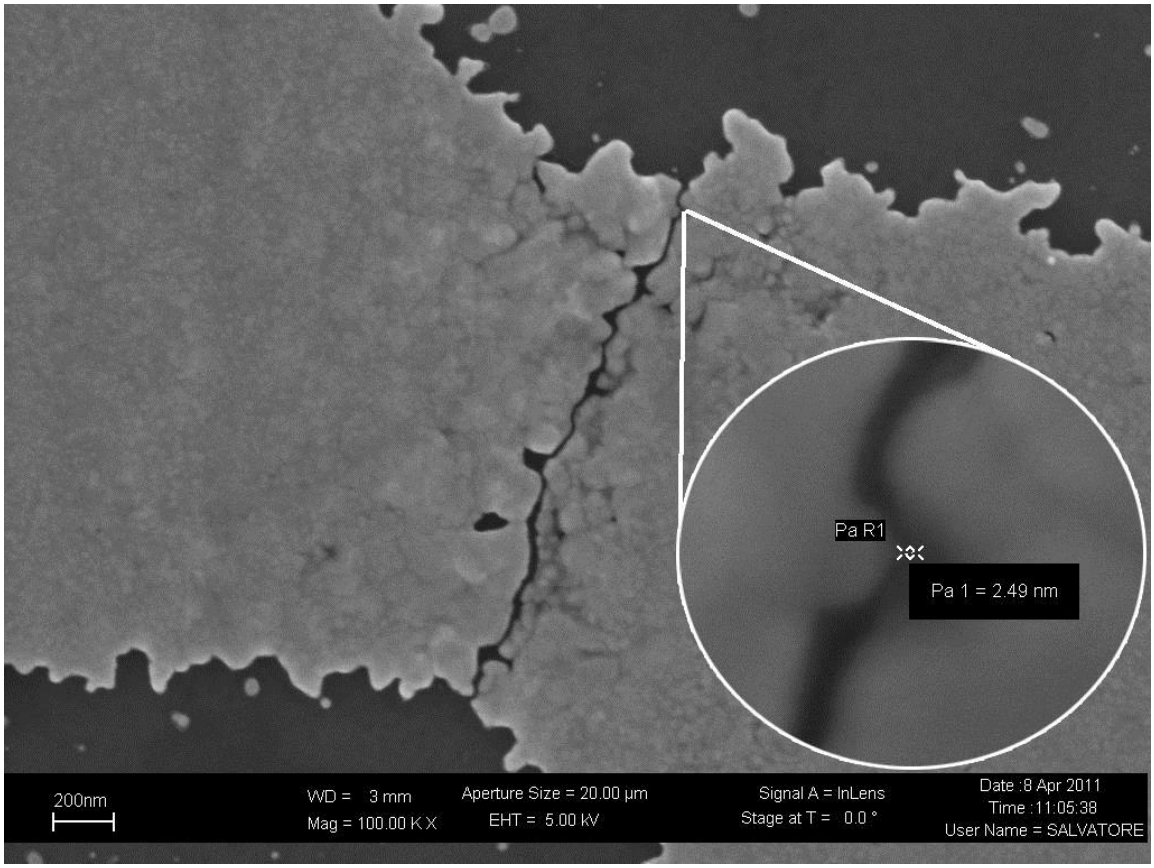

Figure 8: Nanogap FESEM characterization.

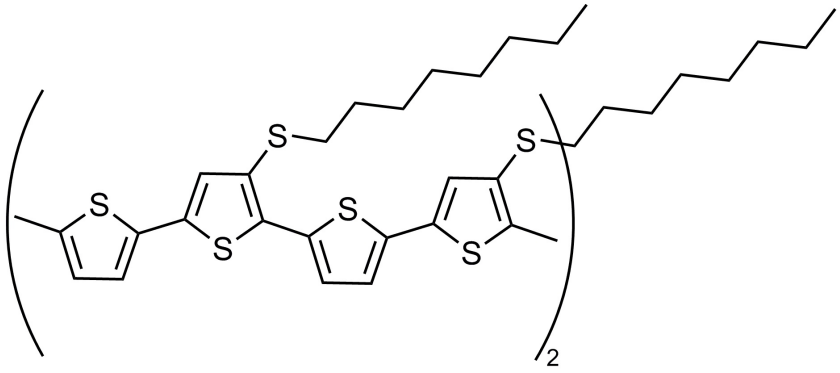

5,5'''-dimethyl-3'',4-bis(octylthio)-2,2':5',2'':5'',2'''-quaterthiophene

Figure 9: The Octithiophene molecule used as molecular wire

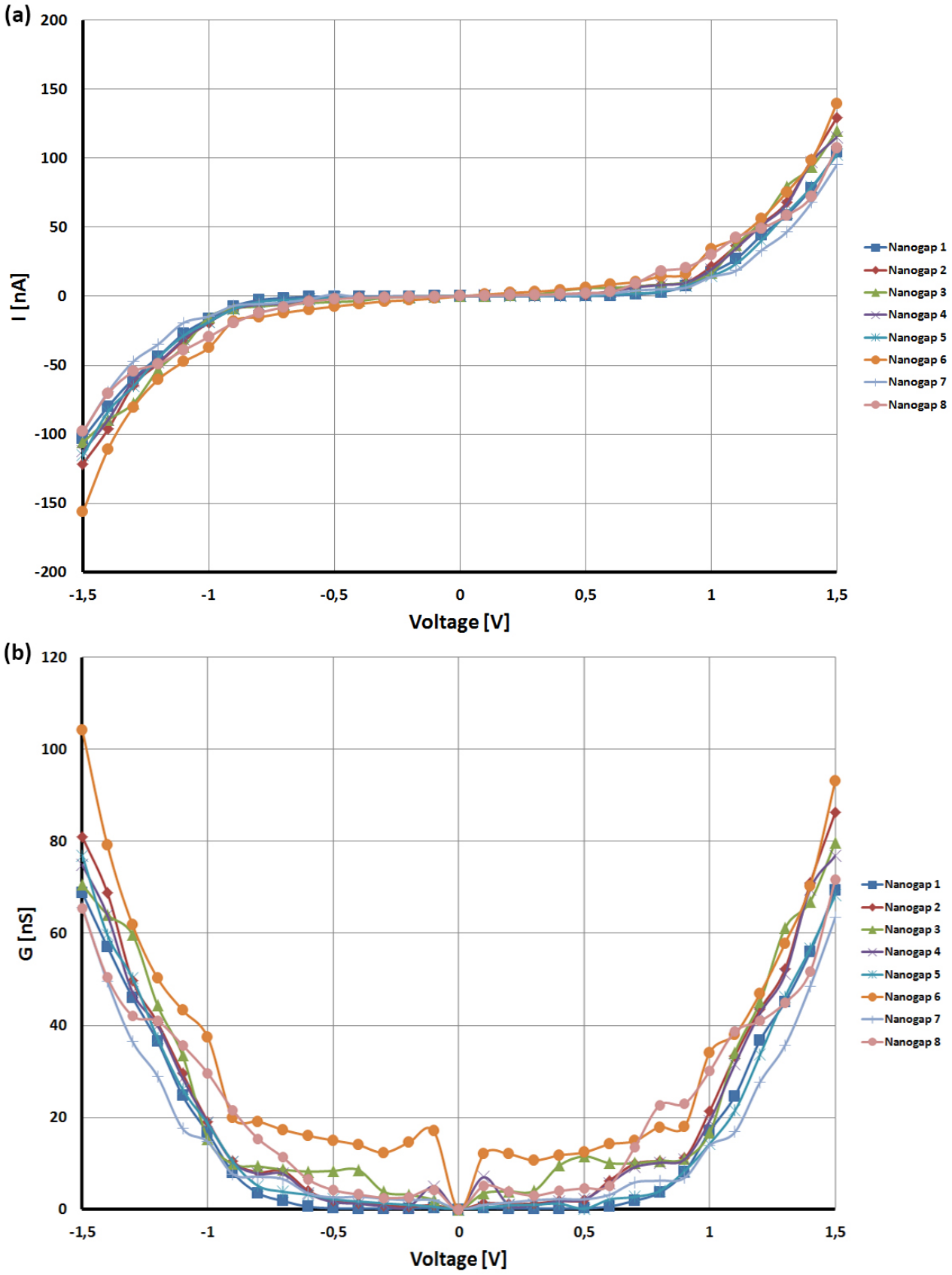

Figure 10: (a) I/V curve and (b) conductance G of the octithiophenes inside 8 different nanogaps

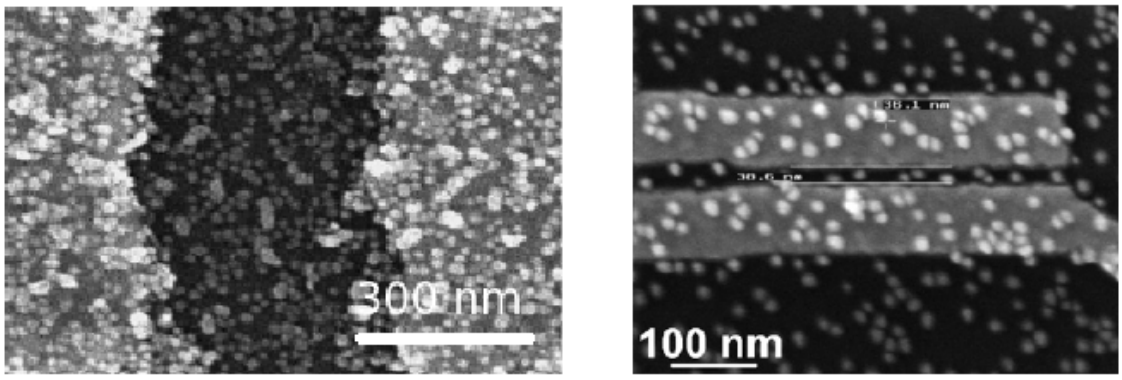

(a) (b)

Figure 11: a) Multilayer of gold nanoparticles between two electrodes [83] b) Complex of antigen/antibody labeled with gold nanoparticles between two electrodes [85].

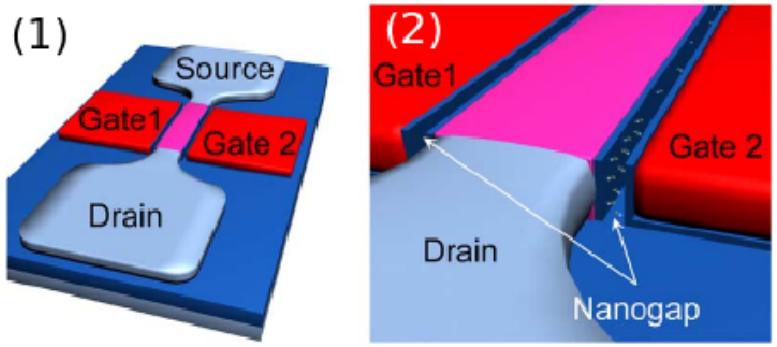

(a)

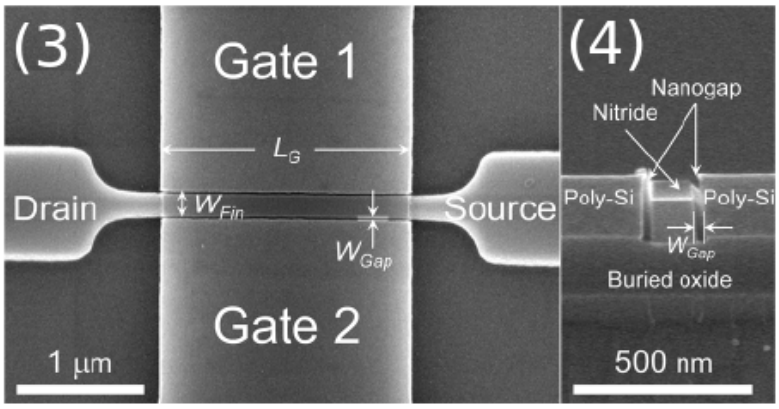

(b)

Figure 12: a.1) Schematic diagrams of a nanogap-embedded separated double gate field effect transistor. a.2) Magnified view of two nanogaps near the drain side. b.3) SEM top view of the nanogap-embedded separated double-gate field effect transistor; b.4) cross-sectional view of etched nanogaps in SEM patterns. [89]

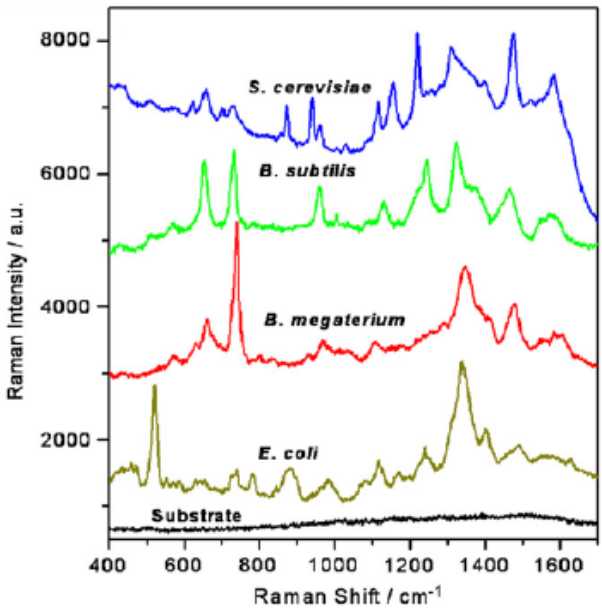

Figure 13: SERS spectra of four kinds of microorganisms obtained from the Ag SERS-active substrate. [93]

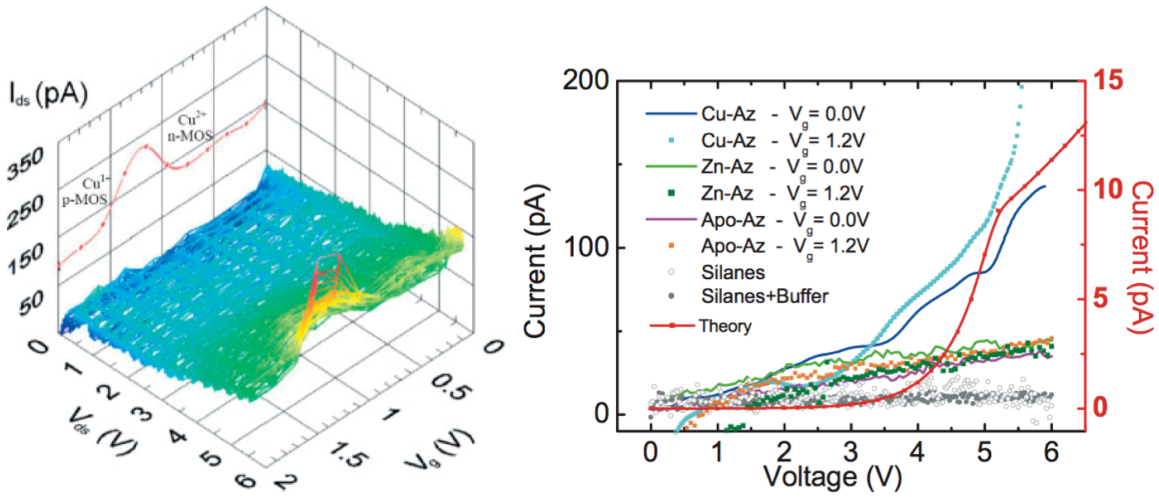

Figure 14: 3D plot of the source-drain current (I_{ds}) as a function as the source-drain voltage (V_{ds}) and the gate voltage (V_g) is shown on the left. A resonant peak arises at V_g = 1.25 V, which separates the regions of the Cu^{-1} p-MOS and Cu^{2+} n-MOS behaviors. On the right source-drain characteristics of different forms of azurin are shown for comparison. [100]

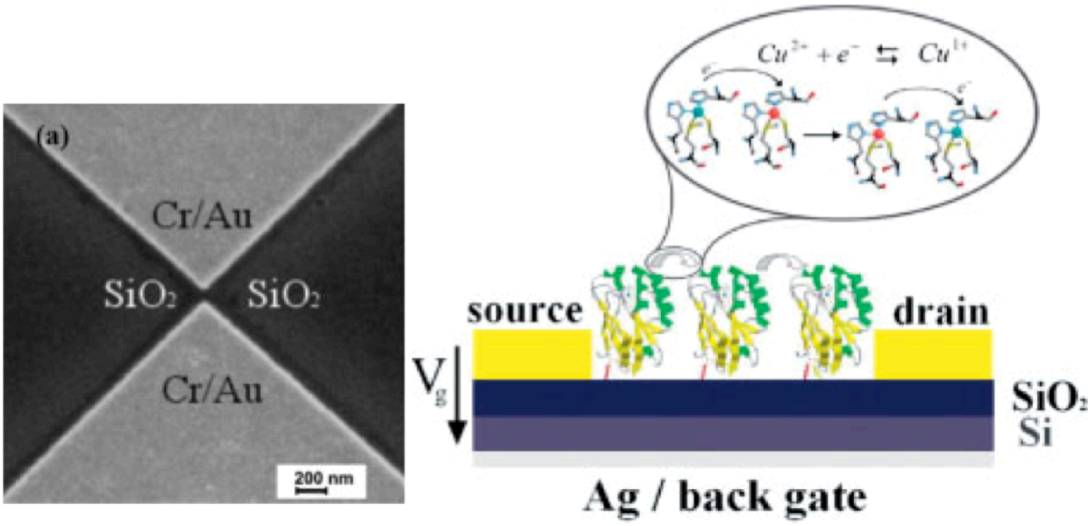

Figure 15: SEM image of the nanogap on the left. The schematic section on the right shows the sequential hopping through azurin molecules, which determines source-drain conduction. V_g at the Ag/back gate electrode modulates the conduction inside the nanogap. [100]

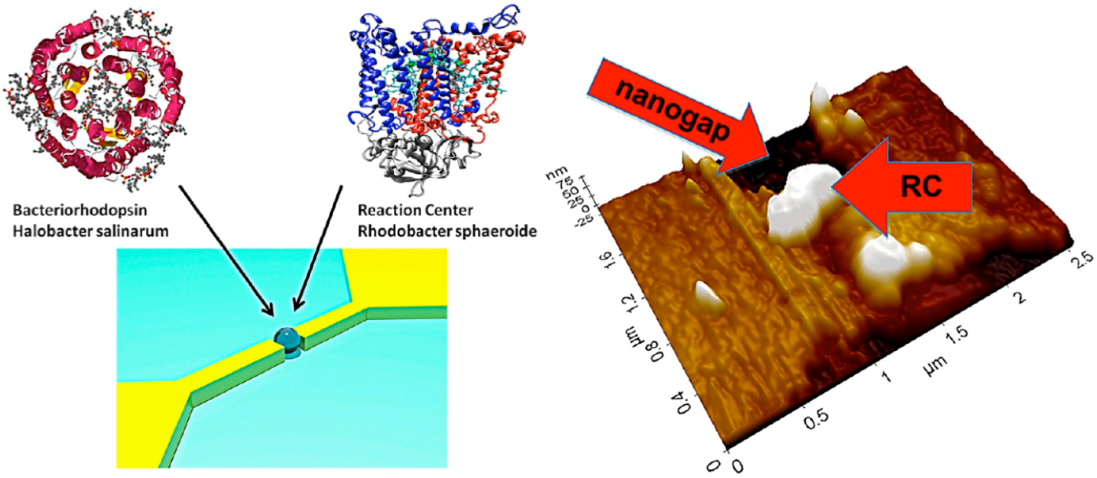

Figure 16: Schematic image of the protein-nanogap molecular junction on the left. AFM image of the RC bridging the nanogap on the right. [101]

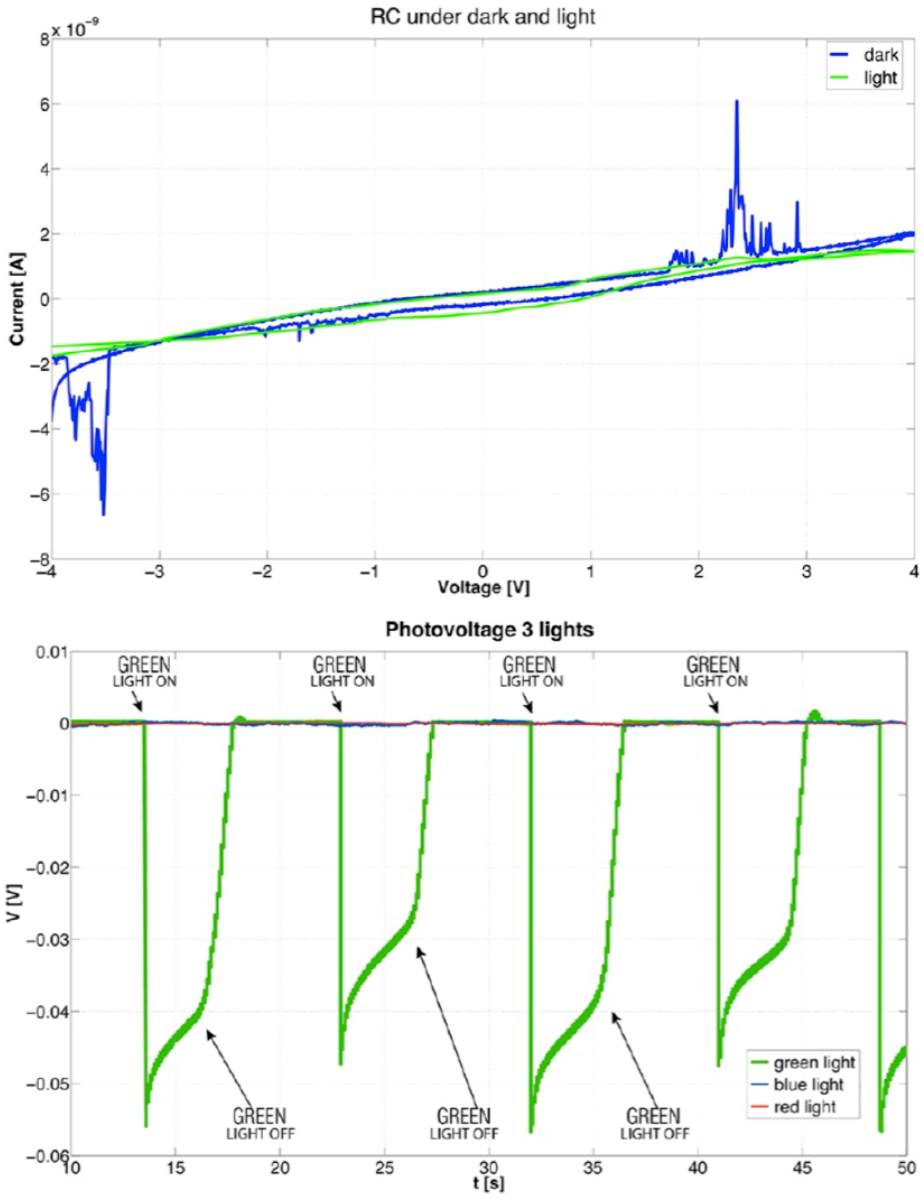

Figure 17: Upper image shows the I/V characteristic of RC-nanogap junction for different conditions of illumination. Lower image shows the photo-generated voltage in BR-nanogap junction for different wavelengths of the incident light. [101]

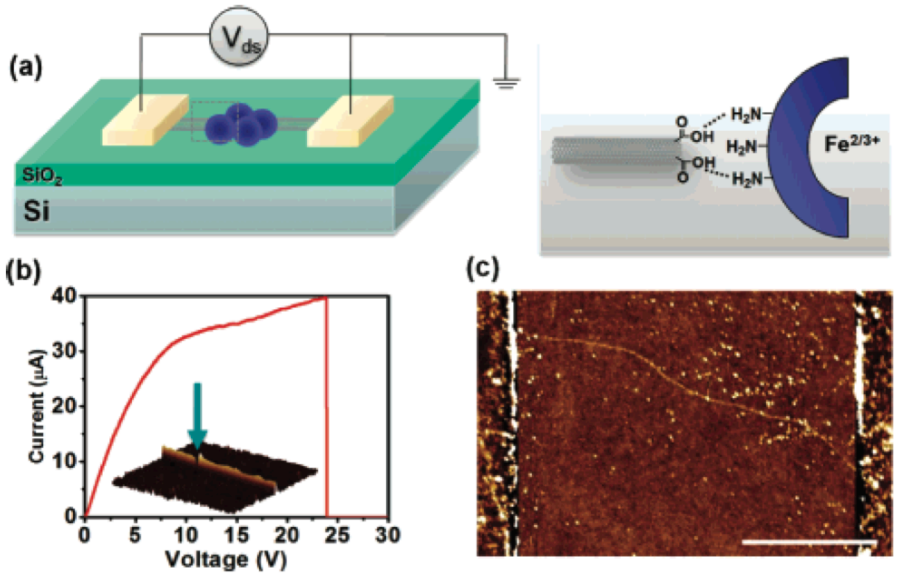

Figure 18: (a) Schematic image of a carbon nanotube based nanogap-protein molecular junction on the left, the chemical bond between the nanogap and the ferritin on the right. (b) Electrical cutting I/V fabrication characteristic and the AFM image of the resulting nanogap. (c) AFM image of ferritin molecules drop casted all over the carbon nanotube. [102]

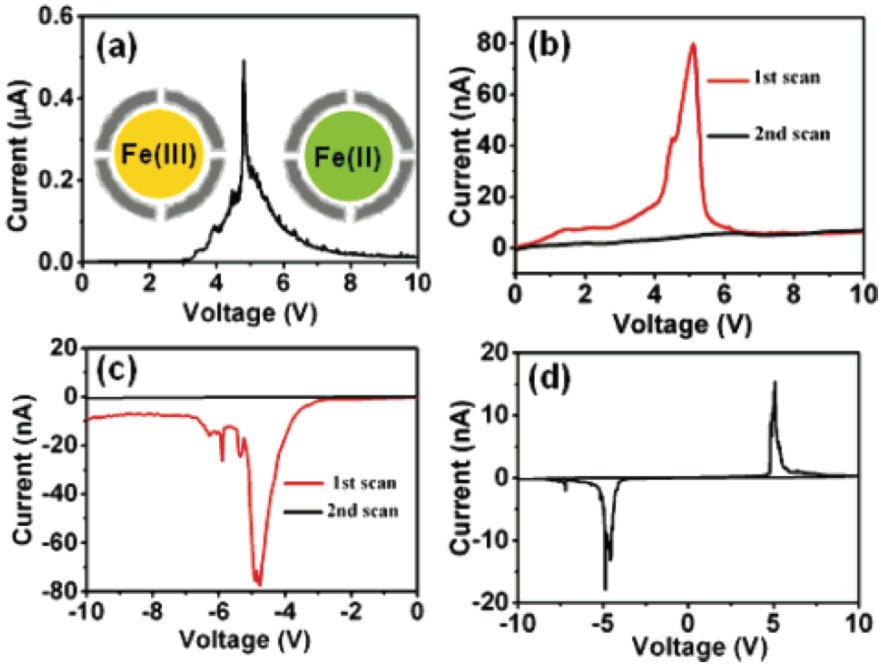

Figure 19: (a) Measured NDR signature, the peak divides two different redox state of the ferritin iron. (b, c, d) Hysteretic I/V characteristics of the molecular junction at different magnifications. [102]

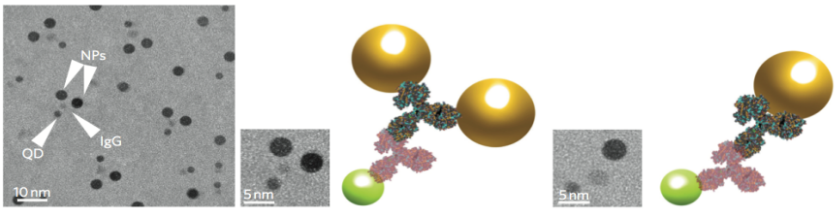

Figure 20: TEM and schematic images showing the Pro-T + QD-IgG' molecules. The biological part consists of 2 antibodies in the center, while gold nanoparticles bind the Fab domains of the primary antibody and a CdSe quantum dot binds the F_c domain of the secondary antibody. [103]

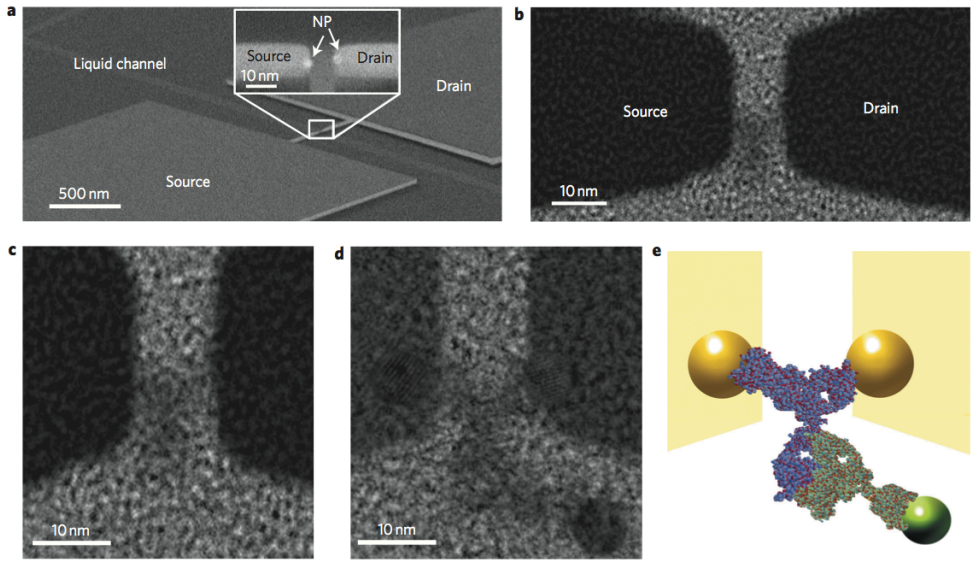

Figure 21: SEM (a) and TEM (b) images of the nanogap-Pro-T molecular junction. TEM images of the Pro-T (c) and Pro-T + QD-IgG' (d) molecular junctions. (e) Schematic image of the molecular junction. [103]

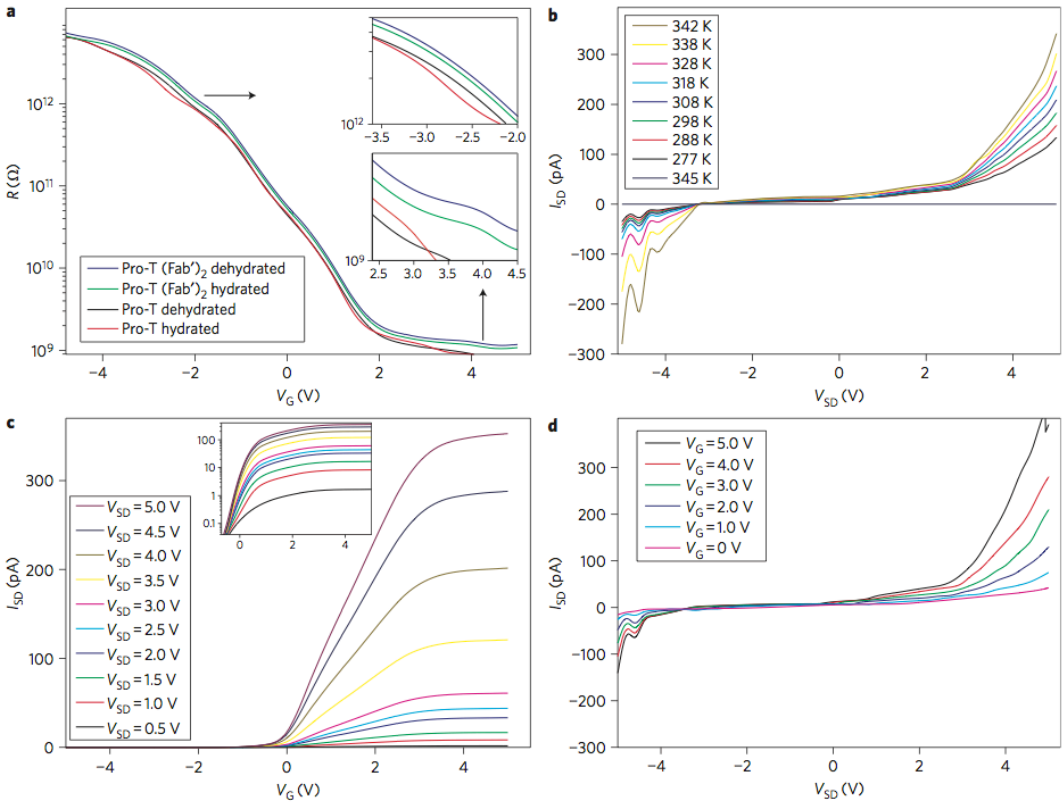

Figure 22: (a) Effect of the hydration on the output resistance. (b) Effect of the temperature on the source-drain characteristic. (c, d) Transconductance and output resistance characteristics of the nanogap-Pro-T based transistor respectively. [103]

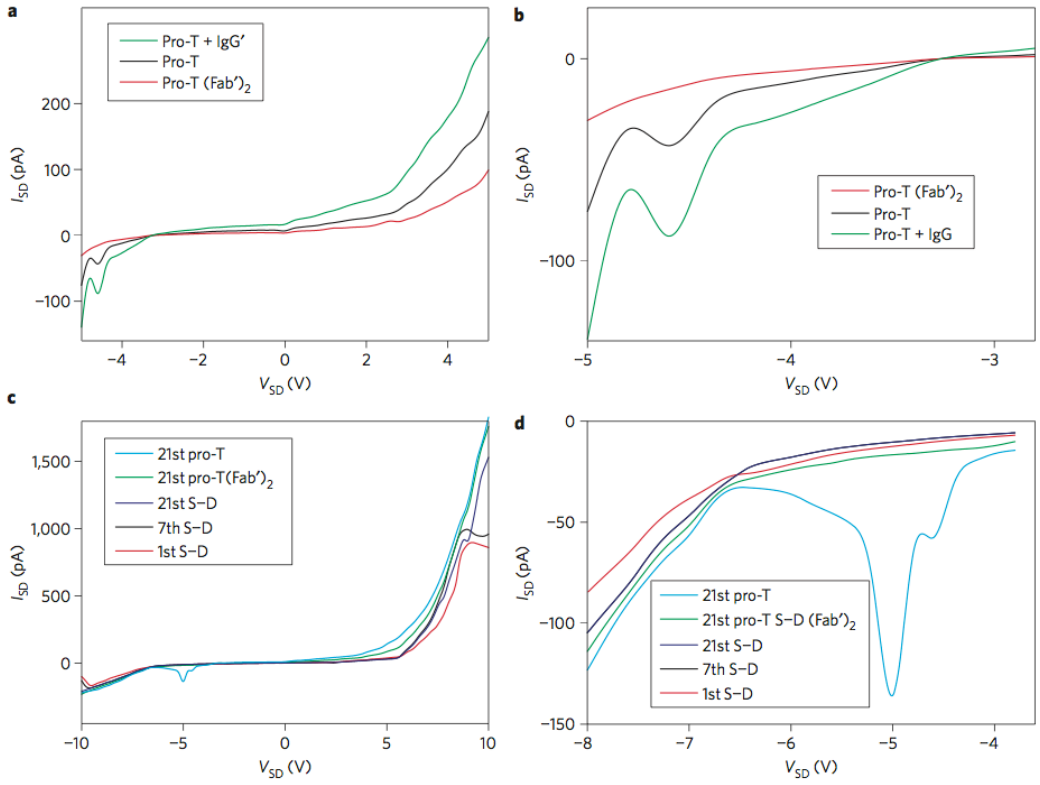

Figure 23: NDR signature for three forms of the Pro-T molecule at two different magnifications. The peak vanishes by removing the F_c domain in the Pro-T (Fab')$_2$, whereas it enhances when 2 F_c domains are present in the Pro-T + IgG'. [103]

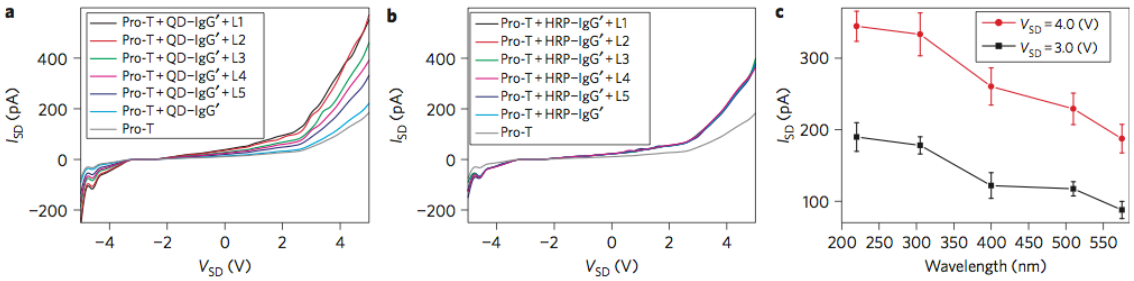

Figure 24: (a) Modulation of the source-drain characteristic of Pro-T + QD-IgG' as a function of five light wavelengths (a) and in presence of HRP (b). (c) Effect of light wavelengths on the current at fixed source-drain bias. [103]

References

[1] Z. K. Keane, J. W. Ciszek, J. M. Tour, D. Natelson, Nano Letters, 6, 1518-1521 (2006).
[2] K. Moth-Poulsen, T. Bjrnholm, Nat. Nanotech., 4, 551-556 (2009).
[3] X. Y. Zhu, Surf. Sci. Rep., 56, 1-83 (2004).
[4] J. R. Heath, M. A. Ratner, Phys. Today 2003, 56, 43.
[5] A. Kornyshev, A. M. Kuznetsov, J. Ulstrup, Proc. Natl. Acad. Sci. USA 2006, 103, 6799.
[6] R. M. Metzger, B. Chen, U. Hopfner, M. V. Lakshmikantham, D. Vuillaume, T. Kawai, X. L. Wu, H. Tachibana, T. V. Hughes, H. Sakurai, J. W. Baldwin, C. Hosch, M. P. Cava, L. Brehmer, G. J. Ashwell, J. Am. Chem. Soc. 1997, 119, 10455.
[7] C. P. Collier, G. Mattersteig, E. W. Wong, Y. Luo, K. Beverly, J. Sampaio, F. M. Raymo, J. F. Stoddart, J. R. Heath, Science 2000, 289, 1172.
[8] A. S. Blum, J. G. Kushmerick, D. P. Long, C. H. Patterson, J. C. Yang, J. C. Henderson, Y. X. Yao, J. M. Tour, R. Shashidhar, B. R. Ratna, Nat. Mater. 2005, 4, 167.
[9] H. Park, J. Park, A. K. L. Lim, E.H. Anderson, A. P. Alivisatos, P. L. McEuen, Nature 2000, 407, 57.
[10] S. Kubatkin, A. Danilov, M. Hjort, J. Cornil, J. L. Bredas, N. Stuhr-Hansen, P. Hedegard, T. Bjørnholm, Nature 2003, 425, 698.
[11] L. H. Yu, D. Natelson, Nano Letters 2004, 4, 79.
[12] C. Kergueris, J. P. Bourgoin, S. Palacin, D. Esteve, C. Urbina, M. Magoga, C. Joachim, Phys. Rev. B 1999, 59, 12505.
[13] M. S. M. Saifullah, T.Ondarcuhu, D. K. Koltsov, C. Joachim,M. E.Welland, Nanotechnology 2002, 13, 659.
[14] W. J. Liang, M. P. Shores, M. Bockrath, J. R. Long, H. Park, Nature 2002, 417, 725.
[15] Q. Qing, F. Chen, P. G. Li, W. H. Tang, Z. Y. Wu, Z. F. Liu, Angew. Chem. Int. Ed. 2005, 44, 7771.
[16] T. Nagase, T. Kubota, S. Mashiko, Thin Solid Films 2003, 438, 374.
[17] C.A. Martin, D. Ding, H. S. J. van der Zant, J. M. van Ruitenbeek, New J. Phys. 2008, 10, 065008
[18] M. A. Reed, C. Zhou, C. J. Muller, T. P. Burgin, J. M. Tour, Science 1997, 278, 252
[19] W. Chen, H. Ahmed, K. Nakazoto, Appl. Phys. Lett. 1995, 66, 3383.
[20] A. F. Morpurgo, C. M. Marcus, D. B. Robinson, Appl. Phys. Lett. 1999, 74, 2084.
[21] J. Park, A. N. Pasupathy, J. I. Goldsmith, C. Chang, Y. Yaish, J. R. Petta, M. Rinkoski, J. P. Sethna, H. D. Abruna, P. L. McEuen, D. C. Ralph, Nature 2002, 417, 722.
[22] A. Notargiacomo, V. Foglietti, E. Cianci, G. Capellini, M. Adami, P. Faraci, F. Evangelisti, C. Nicolini, Nanotechnology 1999, 10, 458.
[23] L. D. Qin, S. Park, L. Huang, C. A. Mirkin, Science 2005, 309, 113.
[24] A. Hatzor, P. S. Weiss, Science 2001, 291, 1019.
[25] H. Park, A. K. L. Lim, A. P. Alivisatos, J. Park, P. L. McEuen, Appl. Phys. Lett. 1999, 75, 301.
[26] D. R. Strachan, D. E. Smith, D. E. Johnston, T. H. Park, M. J. Therien, D. A. Bonnell, A. T. Johnson, Appl. Phys. Lett. 2005, 86, 043109.
[27] A. K. Mahapatro, J. Ying, T. Ren, D. B. Janes, Nano Letters 2008, 8, 2131.
[28] S. Ghosh, H. Halimun, A. K. Mahapatro, J. Choi, S. Lodha, D. Janes, Appl. Phys. Lett. 2005, 87, 233 509.
[29] M. F. Lambert, M. F. Goffman, J. P. Bourgoin, P. Hesto, Nanotechnology 2003, 14, 772.
[30] K. I. Bolotin, F. Kuemmeth, A. N. Pasupathy, D. C. Ralph, Nano Letters 2006, 6, 123.
[31] H. Park, A. K. L. Lim, A. P. Alivisatos, J. Park, P. L. McEuen, Appl. Phys. Lett. 1999, 75, 301.
[32] D. Demarchi, P. Civera, G. Piccinini, M. Cocuzza, and D. Perrone, Electrochimica Acta 2009, 54, 6003–6009.
[33] I. Rattalino, P. Motto, G. Piccinini, D. Demarchi, Physics Letters A 06/2012; 376(30-31):2134–2140.
[34] P. Motto, A. Dimonte, I. Rattalino, D. Demarchi, G. Piccinini, P. Civera, Nanoscale Research Letters 01/2012; 7(1):113
[35] I. Rattalino, V. Cauda, P. Motto, T. Limongi, G. Da, L. Razzari, F. Parenti, E. Di Fabrizi, A. Mucci, L. Schenetti, G. Piccinini, D. Demarchi, RSC Adv. 10/2012; 2(29):10985-10993.
[36] H. B. Yu, Y. Luo, K. Beverly, J. F. Stoddart, H. R. Tseng, J. R. Heath, Angew. Chem. Int. Ed. 2003, 42, 5706

[37] J.R. Black, IEEE Trans. Electron Devices 16 (1969) 338.
[38] D.E. Johnston, D.R. Strachan, A.T.C. Johnson, Nano Letters 7 (2007) 2774.
[39] R.L. De Orio, H. Ceric, S. Selberherr, Microelectron. Reliab. 50 (2010) 775.
[40] M. Schimschak, J. Krug, Comput. Phys. 188 (2003) 640.
[41] A. Averbuch, M. Israeli, M. Nathan, I. Ravve, Phys. Rev. Lett. 78 (1997) 278.
[42] T.O. Ortugani, A. Celik, E.E. Oren, Thin Solid Films 515 (2007) 2974.
[43] M. Khenner, A. Averbuch, M. Israeli, M. Nathan, J. Comput. Phys. 170 (2001) 764.
[44] T.O. Ortugani, E.E. Oren, Int. J. Solids Struct. 42 (2005) 3918.
[45] M. Ohring, J. Appl. Phys. 42 (1971) 2653.
[46] W.W. Mullins, J. Appl. Phys. 28 (1957) 333.
[47] R. Rosenberg, M. Ohring, J. Appl. Phys. 42 (1971) 5671.
[48] M. L. Trouwborst, S. J. V. Molen, B.J. Wees, J. Appl. Phys., vol. 99, no. 11, pp. 114 316–114 316–7, 2006.
[49] K.C.Chen, W.W.Wu, C.N.Liao, L.J.Chen, and K.N.Tu, J. Appl. Phys., vol. 321, no. 5892, pp. 1066–1069, Aug. 2008.
[50] D. R. Strachan, D. E. Johnston, B. S. Guiton, S. S. Datta, P. K. Davies, D. A. Bonnell, A. T. C. Johnson, Phys. Rev. Lett., vol. 100, no. 5, pp. 056 805–056 809, Feb. 2008.
[51] T. O. Ogurtani, E. E. Oren, International Journal of Solids and Structures, vol. 42, no. 13, pp. 3918–3952, June 2005.
[52] M. Ohring, J. Appl. Phys., vol. 42, no. 7, pp. 2653– 2661, Apr. 1971.
[53] E. Clementi, D. L. Raimondi, W. P. Reinhardt, J. Chem. Phys., vol. 47, no. 4, pp. 1300–1307, Apr. 1967.
[54] L. D. L. S. Valladares, A. B. Domnguez, T. Mitrelias, C. H. W. Barnes, J. A. Aguiar, Y. Majima, Vistas in Nanofabrication, 2012.
[55] D. R. Strachan, D. E. Smith, D. E. Johnston, T.-H. Park, M. J. Therien, D. A. Bonnell, A. Johnson, Applied Phisics Letters, vol. 86, p. 043109, 2005.
[56] I. A. Blech, Journal of Applied Physic, vol. 47, no. 4, pp. 1203–1208, 1976.
[57] I. A. Blech and C. Herring, Applied Phisics Letters, vol. 29, no. 3, pp. 131–133, 1976.
[58] I. A. Blech and K. L. Tai, Applied Phisics Letters, vol. 30, no. 8, pp. 387–785 389, 1977.
[59] S. Datta, Quantum Transport: Atom to Transistor. Cambridge University Press, 2005.
[60] Z. K. Keane, J. W. Ciszek, J. M. Tour, D. Natelson, Nano Lett. 2006, 6, 1518.
[61] E. A. Osorio, K. O'Neill, N. Stuhr-Hansen, O. F. Nielsen, T. Bjørnholm, H. S. J. van der Zant, Adv. Mater. 2007, 19, 281.
[62] W. P. Hu, J. Jiang, H. Nakashima, Y. Luo, Y. Kashimura, K. Q. Chen, Z. Shuai, K. Furukawa, W. Lu, Y. Q. Liu, D. B. Zhu, K. Torimitsu, Phys. Rev. Lett. 2006, 96, 027 801.
[63] J. W. Park, A. N. Pasupathy, J. I. Goldsmith, A. V. Soldatov, C. Chang, Y. Yaish, J. P. Sethna, H. D. Abruna, D. C. Ralph, P. L. McEuen, Thin Solid Films 2003, 438, 457.
[64] G. Maruccio, P. Visconti, V. Arima, S. D'Amico, A. Blasco, E. D'Amone, R. Cingolani, R. Rinaldi, S. Masiero, T. Giorgi, G. Gottarelli, Nano Lett. 2003, 3, 479.
[65] R. V. Seidel, A. P. Graham, J. Kretz, B. Rajasekharan, G. S. Duesberg, M. Liebau, E. Unger, F. Kreupl, W. Hoenlein, Nano Lett. 2005, 5, 147.
[66] T. Oike, T. Kurata, K. Takimiya, T. Otsubo, Y. Aso, H. Zhang, Y. Araki, O. Ito, J. Am. Chem. Soc., 127, 15372, (2005).
[67] H.G.O. Sandberg, G.L. Frey, M.N. Shkunov, H. Sirringhaus, R.H. Friend, M.M. Nielsen, C. Kumpf, Langmuir, 18, 10176, (2002).
[68] V.S. Cocoletzi, L.A. Galicia-Luna, O. Elizalde-Solis, J. Chem. Eng. Data, 50, 1631, (2005).
[69] A. Forni, M. Sironi, M. Raimondi, D.L. Cooper, J. Gerratt, J. Phys. Chem. A 101, 4437, (1997).
[70] M.A. Reed, J. Chen, A.M. Rawlett, D.W. Price, J.M. Tour, Appl. Phys. Lett., 78, 3735, (2001).
[71] Y. Zhang, Y. Ye, Y. Li, X. Yin, H. Liu, J. Zhao, THEOCHEM, 802, 53-58, (2007).
[72] R. Yamada, H. Kumazawa, T. Noutoshi, S. Tanaka, and H. Tada, Nano Letters, 8, 1237-1240, (2008).
[73] M. J. Marton, Nat. Med. 1998, 4, 1293.
[74] G. Marazza, I. Chianella, M. Mascini, Biosens. Bioelectron. 1999,14,43.
[75] K. A. Defillipo, M. L. Grayeski Anal. Chim. Acta. 1991, 249, 155.
[76] N. C. Tansil, Z. Gao Nano Today 2006, 1, 28.

[77] S. Hashioka, M. Saito, E. Tamiya, H. Matsumura Appl. Phys. Lett. 2004, 85, 687-689.
[78] K. Doi, Y. Nishioka, S. Kawano, Comput. Theor. Chem. 2012, 999, 203-214.
[79] S. Roy, X. Chen, M.-H. Li, Y. Peng, F. Anariba, Z. Gao, J. Am. Chem. Soc. 2009, 131 (34), 12211-12217.
[80] C.-H. Kim, C. Jung, K.-B. Lee, H. G. Park, Y.-K. Choi, Nanotechnology 2011, 22, 135502 (5pp).
[81] W. Shen, H. Deng, Y. Ren, Z. Gao, Biosens. Bioelectron. 2013, 43, 165-172.
[82] X. Liang, S. Y. Chou, Nano Lett. 2008, 8 (5), 1472-1476.
[83] K.S. Chang, C.K. Chang, S.F. Chou, C.Y. Chen, Biosensors and Bioelectronics, Volume 22, Issue 12, 15 June 2007, Pages 2914-2920.
[84] K. V. Singh, D. K. Bhura, G. Nandamuri, A. M. Whited, D. Evans, J. King, R. Solanki, Langmuir, Volume 27, Issue 22, 23 September 2011 Pages 13931-13939
[85] L. Marcon, O. Melnyk, D. Stialvenard, Biosensors and Bioelectronics, Volume 23, Issue 7, 28 February 2008, Pages 1185-118.
[86] S.K.Kim, H. Cho, H.J. Park, D. Kwon, J.M.Lee, B.H.Chung, Nanotechnology, Volume 20, Issue 45, 13 October 2009
[87] C.S. Lee, S.K.Kim, M. Kim, Sensors, Volume 9, 2009, Pages 7111- 7131.
[88] B. Gu, T.J.Park, J.H. Ahn, X.J. Huang, S..Y. Lee,Y.K. Choi, Small, Volume 5, Issue 21, 2009, Pages 2407-2412.
[89] M. Im, J.H. Ahn, J.W. Han, T.J.Park, S.Y.Lee, Y.K. Choi, IEEE Sensors Journal, Volume 11, Number 2, February 2011, Pages 351-360.
[90] J.M. Choi, J.W. Han, S.j. Choi, Y.K. Choi, IEEE Transactions on electron devices, Volume 57, Issue 12, December 2010, Pages 3477-3484.
[91] K. D. Alexander, K. Skinner, S. Zhang, H. Wei, R. Lopez, Nano Letters Volume 10, 5 October 2010, Pages 4488-4493
[92] W. E. Smith, Chem. Soc. Rev., Volume 37, 2008, Pages 955-964
[93] J. Chen, G. Qin, J. Wang, J. Yu, B. Shen, S. Li, Y. Ren, L. Zuo, W. Shen, B. Das, Biosensors and Bioelectronics, Volume 44, 15 June 2013, Pages 191-197
[94] A. Alessandrini, P. Facci (2007), Metalloproteins Electronics, in S. E. Lyshevski, Nano and Molecular Electronics Handbook, chapter 14, Rochester Institute of Technology, New York, USA: CRC Press.
[95] A. Artzy-Schnirman, E. Brod, M. Epel, M. Dines, T. Hammer, I. Benhar, Y. Reiter, U. Sivan, Nano Letters, 15, 2008, 3398-3403.
[96] A. Alessandrini, M. Salerno, S. Frabboni, P. Facci, Appl. Phys. Lett., 86, 2005, 133902.
[97] J. J. Davis, N. Wang, A. Morgan, T. Zhang, J. Zhao, Farad. Discuss., 131, 2006, 167-179.
[98] E. D. Mentovich, B. Belgorodsky, S. Richter, J. Phys. Chem. Lett., 2, 2011, 1125-1128.
[99] K.J. Gan, C.S. Tsai, D.S. Liang, Analog. Integr. Circ. Sig. Process., 62, 2010, 63-68.
[100] G. Maruccio, A. Biasco, P. Visconti, A. Bramanti, P.P.Pompa, F. Calabi, R. Cingolani, R. Rinaldi, S. Corni, R. Di Felice, E. Molinari, M. P. Verbeet, G. W. Canters, Adv. Mater., 17, 2005, 816-822.
[101] A. Dimonte, S. Frache, V. Erokhin, G. Piccinini, D. Demarchi, F. Milano, G. De Micheli, S. Carrara, BioMacroMolecules, 13, 2012, 3503-3509.
[102] Q. Tang, H.K. Moon, Y. Lee, S. M. Yoon, H. J. Song, H. Lim, H. C. Choi, J. Am. Chem. Soc., 129, 2007, 11018-11019.
[103] Y.S. Chen, M.Y. Hong, G.S. Huang, Nat. Nanotechnol., 7, 2012, 197-203.